NOTICE

The quality of this microform is heavily dependent upon the quality of the original thesis submitted for microfilming. Every effort has been made to ensure the highest quality of reproduction possible.

If pages are missing, contact the university which granted the degree.

Some pages may have indistinct print especially if the original pages were typed with a poor typewriter ribbon or if the university sent us an inferior photocopy.

AVIS

La qualité de cette microforme dépend grandement de la qualité de la thèse soumise au microfilmage. Nous avons tout fait pour assurer une qualité supérieure de reproduction.

S'il manque des pages, veuillez communiquer avec l'université qui a conféré le grade.

La qualité d'impression de certaines pages peut laisser à désirer, surtout si les pages originales ont été dactylographiées à l'aide d'un ruban usé ou si l'université nous a fait parvenir une photocopie de qualité inférieure.

Canadä

UNIVERSITY OF ALBERTA

A KINETIC STUDY OF THE REDUCTION OF N_2O AND NO BY CO ON
A PLATINUM CATALYST USING STEADY-STATE BIFURCATION AND
FORCED COMPOSITION CYCLING TECHNIQUES

BY

RAMAKANT R. SADHANKAR

©

A THESIS
SUBMITTED TO THE FACULTY OF GRADUATE STUDIES AND RESEARCH
IN PARTIAL FULFILMENT OF THE REQUIREMENTS FOR THE DEGREE OF
DOCTOR OF PHILOSOPHY

DEPARTMENT OF CHEMICAL ENGINEERING

EDMONTON, ALBERTA
SPRING 1995

THE AUTHOR HAS GRANTED AN
IRREVOCABLE NON-EXCLUSIVE
LICENCE ALLOWING THE NATIONAL
LIBRARY OF CANADA TO
REPRODUCE, LOAN, DISTRIBUTE OR
SELL COPIES OF HIS/HER THESIS BY
ANY MEANS AND IN ANY FORM OR
FORMAT, MAKING THIS THESIS
AVAILABLE TO INTERESTED
PERSONS.

L'AUTEUR A ACCORDE UNE LICENCE
IRREVOCABLE ET NON EXCLUSIVE
PERMETTANT A LA BIBLIOTHEQUE
NATIONALE DU CANADA DE
REPRODUIRE, PRETER, DISTRIBUER
OU VENDRE DES COPIES DE SA
THESE DE QUELQUE MANIERE ET
SOUS QUELQUE FORME QUE CE SOIT
POUR METTRE DES EXEMPLAIRES DE
CETTE THESE A LA DISPOSITION DES
PERSONNE INTERESSEES.

THE AUTHOR RETAINS OWNERSHIP
OF THE COPYRIGHT IN HIS/HER
THESIS. NEITHER THE THESIS NOR
SUBSTANTIAL EXTRACTS FROM IT
MAY BE PRINTED OR OTHERWISE
REPRODUCED WITHOUT HIS/HER
PERMISSION.

L'AUTEUR CONSERVE LA PROPRIETE
DU DROIT D'AUTEUR QUI PROTEGE
SA THESE. NI LA THESE NI DES
EXTRAITS SUBSTANTIELS DE CELLE-
CI NE DOIVENT ETRE IMPRIMES OU
AUTREMENT REPRODUITS SANS SON
AUTORISATION.

ISBN   0-612-01759-1

Canada

UNIVERSITY OF ALBERTA

RELEASE FORM

NAME OF AUTHOR: Ramakant Raghunathrao Sadhankar

TITLE OF THESIS: A Kinetic Study of the Reduction of N_2O and NO by CO on a Platinum Catalyst using Steady-State Bifurcation and Forced Composition Cycling Techniques.

DEGREE: Doctor of Philosophy

YEAR THIS DEGREE GRANTED: 1995

Permission is hereby granted to the University of Alberta Library to reproduce single copies of this thesis and to lend or sell such copies for private, scholarly or scientific purposes only.

The author reserves all other publication and other rights in association with the copyright in the thesis, and except as hereinbefore provided neither thesis nor any substantial portion thereof may be printed or otherwise reproduced in any material form whatever without the author's prior written permission.
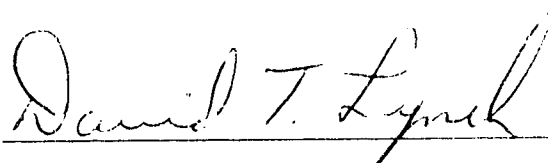
8407 - 14th Avenue

Edmonton, Alberta T6K 1X3

Date: February 28 , 1995

UNIVERSITY OF ALBERTA

FACULTY OF GRADUATE STUDIES AND RESEARCH

The undersigned certify that they have read, and recommend to the Faculty of Graduate Studies and Research for acceptance, a thesis entitled A KINETIC STUDY OF THE REDUCTION OF N_2O AND NO BY CO ON A PLATINUM CATALYST USING STEADY-STATE BIFURCATION AND FORCED COMPOSITION CYCLING TECHNIQUES submitted by Ramakant Raghunathrao Sadhankar in partial fulfilment of the requirements for the degree of Doctor of Philosophy.

Dr. D.T. Lynch

Dr. R.E. Hayes

Dr. L.D. Schmidt

Dr. J. Takats

Dr. S.E. Wanke

Date: FEBRUARY 23, 1995

DEDICATION

This thesis is dedicated to Emmy, Aaron and Leroy
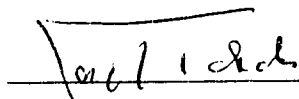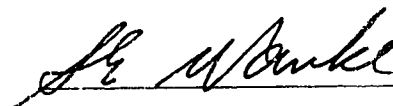
ACKNOWLEDGEMENT

ABSTRACT

The reduction reactions of N_2O and NO by CO over a Pt/Al_2O_3 catalyst have been studied using an external recycle reactor. The N_2O+CO reaction was found to exhibit isothermal steady-state multiplicity at 461-520 K. The steady-state bifurcation behavior has been used to discriminate among four rival mechanisms. Only a kinetic model based on a three-step mechanism and invoking CO self-exclusion from the platinum surface could describe the observed behavior. The model was further tested using transient behavior produced by forced square-wave cycling of CO and N_2O concentrations in the feed. The phase angle between the two square-waves has a pronounced effect on the reaction-rate resonance. Time-average CO conversions as high as five times the steady-state conversion were attained during feed cycling. The model was further modified by incorporating a reaction rate enhancement effect, due to Pt surface phase transition (1x1 ↔ hex), to describe both the transient behavior during feed cycling and the steady-state multiplicity.

The NO+CO reaction also exhibits isothermal steady-state multiplicity at 465-520 K. Generally, the selectivity towards N_2O formation decreased with increasing NO conversion. For the high-conversion steady-states, the N_2O selectivity decreased rapidly with a decrease in the feed $[NO]_o/[CO]_o$ ratio below a critical value of 1.5. It is shown that the N_2O+CO reaction occurs to a significant extent (up to 50%) in the overall NO+CO reaction. The multiplicity behavior and the N_2O selectivity have been described by a seven-step mechanism incorporating the CO self-exclusion effect. The NO+CO reaction also exhibits reaction-rate resonance during variable-phase feed composition cycling. Time-average CO and NO conversions of more than 20 times the steady-state conversions were obtained during feed cycling. The transient results seem to support the seven-step mechanism that was used to describe the steady-state multiplicity. The NO+CO reaction exhibits long-term transients during feed cycling. The number of cycles required to reach cycle-invariance was found to be strongly and inversely dependent on the ratio of the gas-phase capacitance to the surface capacitance.

PREFACE

This thesis is concerned with an examination of the reduction reactions of nitrous oxide and nitric oxide with carbon monoxide. These reactions have been studied because of their importance in automobile catalytic converters. The study involved both experimental and mathematical modelling work. The techniques used for the experimental work involved steady-state bifurcation and forced composition cycling, both of which have been proven to provide a sensitive discrimination among rival reaction mechanisms.

This thesis is organized in a "paper-format" specified in the "Thesis Handbook - A Manual of Regulations and Guide for These Preparation, November 1994" of the Faculty of Graduate Studies and Research. Each of the four chapters following the introductory chapter, namely, Chapters 2-5, is presented in the form of a manuscript without an abstract. The publication details of the manuscripts are given in the footnote of the respective chapter, wherever applicable. The experimental data and the computer programs for mathematical modelling are given in the appendices at the end of the thesis. The bibliography and nomenclature for each chapter appears at the end of the respective chapter. The references to the literature have been cited in the text by italic numerals in parentheses. The citation format is similar to that used by the *Journal of Catalysis*.

TABLE OF CONTENTS

LIST OF TABLES

LIST OF FIGURES

1. INTRODUCTION

1.1 Motivation

The emission of nitrogen oxides (NO_x) from automobile exhaust was recognised as a major source of air-pollution in the early 1950s (*1*). NO_x consists primarily of nitric oxide (NO) and nitrogen dioxide (NO_2) which are produced in all combustion processes by the oxidation of atmospheric nitrogen and fuel-bound nitrogen. NO_2 is linked to causing bronchitis, pneumonia, susceptibility to viral infection and alterations to immune system (*2, 3*). It also contributes to acid rain, urban smog and ozone (*2*). NO_2 is produced from the oxidation of NO, a reaction which proceeds rapidly in sunlight especially in the presence of hydrocarbons (*4*). Therefore, NO is the key starting point in the chain of events leading to various health and environmental concerns described earlier. Thus, if NO is prevented from entering the atmosphere, most of the downstream effects of NO_x pollution can be eliminated. Although NO is produced by lightening and volcanic activity, its main source is the combustion of fossil fuels especially in automobiles and industrial combustors. As early as 1952, two major components of the automobile exhaust, namely, the hydrocarbons (HC) and NO_x were identified as the main contributors to the problem of photochemical smog formation in urban centres (*1*). Because of the smog problem, the U.S. automobile manufacturers began studying the problem of automobile emission in 1953, and in 1957 recognized that the use of an oxidation catalytic converter was a viable approach for reducing HC emissions (*1*).

Automobile catalytic converters were introduced in the U.S. in 1974 to lower the emission of carbon monoxide (CO) and HC (*5*). The NO_x standard of 2 g/mile could be met by using exhaust gas recirculation which leads to the formation of less NO_x in the engine (*6*). Since 1981, more complex control systems have been used in the U.S. in order to satisfy the stricter 1 g/mile emission requirement for NO_x. Increasingly stringent

1

regulations on NO_x have fuelled the search for better catalysts since then. Literally thousands of catalysts have been tested in the laboratories around the world and many have been patented. Presently, all of the automobile converter catalysts contain noble metals, such as platinum, rhodium and palladium. This type of catalyst is called a three-way-catalyst because it simultaneously promotes the conversion of three common pollutants namely, CO, HC and NO_x. NO is selectively reduced by CO in the presence of excess oxygen. The selectivity towards the NO+CO reaction is attributed to the presence of rhodium catalyst in the converter (6). At a typical exhaust gas temperature of 770 K, only rhodium is somewhat favourably selective towards the NO+CO reaction. At a lower temperature of 570 K, both platinum and rhodium are equally selective for the NO+CO reaction (7). To obtain maximum conversion efficiencies for the three pollutants, the air-to-fuel ratio is controlled using a "closed-loop" feed-back control system (5). A large number of reactions occur in the automobile catalytic converter under the actual operating conditions involving HC, CO, NO_x, oxygen (O_2), water and other intermediates. However, the reactions between CO, NO and/or O_2 have been studied extensively to understand the role of the catalyst for simultaneous oxidation (of CO by O_2) and reduction (of NO by CO).

The reduction of NO by CO over noble metal catalysts has been the subject of several studies in the last two decades because of its importance in automobile catalytic converters. These studies were carried out on both single crystals and supported catalysts containing either platinum or rhodium. Several studies revealed very complex phenomena occurring for the platinum-catalyzed NO+CO reaction. The reaction has been shown to exhibit self-sustained oscillations, both on crystalline platinum (8-12) as well as on supported platinum catalysts (13). In addition, the reaction has also been shown to exhibit reaction rate multiplicity on crystalline platinum surfaces (10-12, 14). Temperature programmed reaction studies (15, 18) have revealed the "explosive" nature of the reaction from the rapid evolution of carbon dioxide and nitrogen products in an extremely narrow temperature range. The mechanisms underlying these complex phenomena cannot be explained by simple Langmuir-Hinshelwood kinetics. While the

exact mechanism by which NO is reduced by CO on platinum catalysts has not been completely determined, several studies (19-25) have reported the formation of nitrous oxide (N_2O) as an intermediate in the overall NO+CO reaction, particularly at temperatures below 580 K. At a typical operating temperature of 770 K in an automobile catalytic converter, the overall NO+CO reaction proceeds according to Eq. (1.1).

$$2NO + 2CO \rightarrow 2CO_2 + N_2 \qquad (1.1)$$
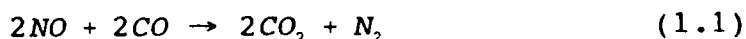
The formation of N_2O at lower temperature, and its subsequent reduction by CO, can be described by the reactions according to Eqs. (1.2) and (1.3), respectively (24).

$$2NO + CO \rightarrow CO_2 + N_2O \qquad (1.2)$$

$$N_2O + CO \rightarrow CO_2 + N_2 \qquad (1.3)$$
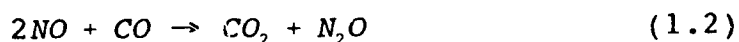
Therefore, the N_2O+CO reaction according to Eq. (1.3) is considered to be an important subset of the overall NO+CO reaction. Despite its importance in the overall NO+CO reaction, the reaction of N_2O with CO on platinum catalyst has rarely been the main focus of an investigation (26, 27). Therefore, this study was undertaken to understand the role of the N_2O formation and other complex phenomena that occur for the platinum catalyzed NO+CO reaction.

1.2 Objective

The main objective of this study is to investigate the platinum catalyzed NO+CO reaction in order to gain an insight into the complex behaviour of the reaction reported in previous studies and to understand the formation of N_2O at low temperatures. Most of the previous work was carried out at high temperatures, where N_2O was not observed or was found in insignificant amounts. As such, the platinum catalyzed N_2O+CO reaction has not previously been thoroughly studied. Therefore, an additional objective of the study is to gain a thorough understanding of the N_2O+CO reaction as a sub-reaction of the overall NO+CO reaction. Finally, it is intended to explain the observed experimental

behavior by appropriate kinetic models.

1.3 Methodology

A step-wise approach has been used in this study. The N_2O+CO reaction has been investigated as a first step in the study of the overall $NO+CO$ reaction. The experiments were performed using an external recycle reactor containing a 0.5 wt% Pt/Al_2O_3 catalyst. All of the experiments were carried out at temperatures below 580 K because of the observations from other studies that N_2O rmation is significant in the $NO+CO$ reaction at these temperatures. Both reactions, namely, the N_2O+CO reaction and the $NO+CO$ reaction, have been investigated using experimental steady-state and transient behavior. The steady-state experiments are concerned with examining isothermal multiplicity behavior, while the transients are generated using feed composition cycling. The steady-state bifurcation behaviour of the reaction can be used for a sensitive discrimination among several rival mechanisms as shown by Graham and Lynch (28) in an earlier study of the platinum-catalyzed CO oxidation. In a later study, Graham and Lynch (29) used the technique of variable-phase feed composition cycling to study the transient behaviour of the $CO+O_2$ reaction and developed a mechanism which consistently described the steady-state bifurcation and the reaction-rate resonance during feed cycling. Because of the apparent similarity between the $CO+O_2$ reaction and the $CO+N_2O$ and $CO+NO$ reactions, the same techniques using steady-state bifurcation and forced composition cycling are employed for this study.

1.4 Outline

This thesis consists of six chapters. This introductory chapter is followed by Chapter 2 which describes the steady-state behaviour of the N_2O+CO reaction. The steady-state multiplicity behaviour of the N_2O+CO reaction has been used to discriminate among four different mechanisms. In Chapter 2, it is shown that only a model based on a CO self-

exclusion (from Pt surface) effect can describe the observed steady-state multiplicity behaviour. In Chapter 3, the transient behaviour of the N_2O+CO reaction during the forced feed cycling has been described. The effect of the cycle frequency and the phase angle between the NO and CO feed cycles on the resonant behaviour of the reaction has been discussed. A kinetic model, described in Chapter 3, provides a consistent explanation for the steady-state multiplicity and the resonance during feed cycling. The fourth chapter describes the steady-state multiplicity behaviour of the NO+CO reaction. The effect of temperature and feed composition on the multiplicity behaviour and the selectivity of the NO+CO reaction towards N_2O formation has been discussed. The steady-state multiplicity and the N_2O selectivity has been described by a kinetic model based on a seven-step reaction mechanism. It is also shown that the N_2O+CO reaction occurs to a substantial extent in the overall NO+CO reaction. In Chapter 5, the transient behaviour of the NO+CO reaction during feed composition cycling has been described. The effect of the feed composition, cycling frequency and the phase angle between the CO and NO feed cycles on the resonance behaviour of the reaction has been discussed. Finally, Chapter 6 summarizes the conclusions of this study and provides some recommendations about future work.

1.5 References

1. Briggs, W.S. in "Applied Industrial Catalysis" (B.E. Leach, Ed.), Vol. 3, p. 241-270 Academic Press Inc. 1984.

2. Chiron, M. in "Catalysis and Automotive Pollution Control: Proceedings of the First International Symposium, Brussels, Sept. 1986" (A. Crucq and A. Frennet, Eds.), p. 1-10, Elsevier Science Publishers, B.V., Amsterdam, 1987.

3. Armor, J.N. in "Environmental Catalysis" (J. N. Armor, Ed.) ACS Symposium Series 552, p. 1-6, American Chemical Society, Washington DC 1994.

4. Impens, R. in "Catalysis and Automotive Pollution Control: Proceedings of the First International Symposium, Brussels, Sept. 1986", (A. Crucq and A. Frennet, Eds.), p. 11-24, Elsevier Science Publishers B.V., Amsterdam 1987.

5.   Taylor, K.C. in "Catalysis Science and Technology" (J.R. Anderson and M. Boudart, Eds.), Vol. 5, p. 119-170, Springer-Verlag, Berlin 1984.

6.   Taylor, K.C. in "Catalysis and Automotive Pollution Control: Proceedings of the First International Symposium, Brussels, Sept. 1986", (A. Crucq and A. Frennet, Eds.), p. 97-116, Elsevier Science Publishers B.V., Amsterdam 1987.

7.   Hahn, T. and Lintz, H.G., *Appl. Surf. Sci.* **40**, 59-63 (1989).

8.   Adlhoch, W. and Lintz, H.G., *Z. Phys. Chemie Neue Folge* **103**, 207-211 (1976).

9.   Adlhoch, W., Lintz, H.G. and Weisker, J., *Surf. Sci.* **103**, 576-585 (1981).

10.   Schwartz, S.B. and Schmidt, L.D., *Surf. Sci.* **183**, L269-L278 (1987).

11.   Schwartz, S.B. and Schmidt, L.D., *Surf. Sci.* **206**, 169-186 (1988).

12.   Fink, Th., Dath, J.P., Imbihl, R. and Ertl, G., *J. Chem. Phys.* **95**, 2109-2126 (1991).

13.   Schüth, F. and Wicke, E. in "Instationary Processes and Dynamic Experimental Methods in Catalysis, Electrochemistry and Corrosion" (G. Sandstede and G. Kreysa, Eds.), Dechema Monogr., Vol. 120, p. 429-441 (1989).

14.   Bolten, H., Hahn, T., LeRoux, J. and Lintz, H.G., *Surf. Sci.* **160**, L529-L532 (1985).

15.   Lesley, M.W. and Schmidt, L.D., *Surf. Sci.* **155**, 215-240 (1985).

16.   Lesley, M.W. and Schmidt, L.D., *Chem. Phys. Lett.* **102**, 459-463 (1983).

17.   Fink, Th., Dath, J.P., Bassett, M.R., Imbihl, R. and Ertl, G., *Vacuum* **41**, 301-303 (1990).

18.   Fink, Th., Dath, J.P., Bassett, M.R., Imbihl, R. and Ertl, G., *Surf.-Sci.* **245**, 96-110 (1991).

19.   Lambert, R.M. and Comrie, C.M., *Surf. Sci.* **46**, 61-80 (1974).

20.   Lorimer, D. and Bell, A.T., *J. Catal.* **59**, 223-238 (1979).

21.   Kudo, A., Steinberg, M., Bard, A.J., Campion, A., Fox, M.A., Mallouk, T.E., Webber, S.E. and White, J.M. **125**, 566-587 (1990).

22.   Solymosi, F., Völgyesi, L. and Sárkány, J., *J. Catal.* **54**, 336-344 (1978).

23.   Adlhoch, W. and Lintz, H.G., *Surf. Sci.* **78**, 58-68 (1978).

24. Shelef, M. and Otto, K., *J. Catal.* **10**, 408-412 (1968).

25. Muraki, H. and Fujitani, Y., *Ind. Eng. Chem. Prod. Res. Dev.* **25**, 414-419 (1986).

26. Adlhoch, W., Kohler, R. and Lintz, H.G., *Z. Phys. Chemie. Neue Folge* **120**, 111-118 (1980).

27. Lintz, H.G., *Surf. Sci.* **108**, L486-L489 (1981).

28. Graham, W.R.C. and Lynch, D.T., *AIChE J.* **33**, 792-800 (1987).

29. Graham, W.R.C. and Lynch, D.T., *AIChE J.* **36**, 1796-1806 (1990).

2. N₂O REDUCTION BY CO:

STEADY-STATE BEHAVIOR*

2.1 Introduction

The reduction reactions of various nitrogen oxides by carbon monoxide over noble metal catalysts have been studied extensively because of their importance in automobile catalytic converters. At a typical exhaust gas temperature of 770 K, while nitric oxide (NO) is present in significant amounts, nitrous oxide (N_2O) is not commonly observed. Therefore, the reduction of NO by CO over noble metal catalysts has been the main focus of several studies. It is been shown that the reduction reaction of NO by CO can exhibit complex behavior such as steady-state multiplicity (*1,2*) and self-sustained oscillations (*2-8*). A catalyst surface reconstruction process for Pt(100) has been suggested (*5-7*) as possibly being responsible for some of the observed complex behavior. While the exact mechanism by which NO is reduced by CO over the supported noble metal catalysts has not been completely determined, several studies (*9-18*) have reported the formation of N_2O as an intermediate in the overall NO+CO reaction, particularly at temperatures below 580 K. Thus, an understanding of the detailed mechanism of the N_2O+CO reaction is necessary in order to understand the complex behavior of the overall NO+CO reaction over supported noble metal catalysts.

Despite the frequent observation of N_2O formation and reaction during the reduction of NO by CO, the reaction of N_2O with CO on noble metal catalysts has only rarely been the primary focus of an investigation (*17, 19-21*). Adlhoch et al.(*19*) found

---

that the rate of the N_2O+CO reaction over polycrystalline platinum is two orders of magnitude lower than the rate of the $NO+CO$ reaction, and that N_2O decomposition is the rate limiting step. Lintz (20) compared the reaction probabilities of the $NO+CO$, N_2O+CO and O_2+CO reactions over polycrystalline platinum and proposed an elementary reaction sequence for the N_2O+CO reaction. McCabe and Wong (17) investigated the kinetics of the N_2O+CO reaction over a supported rhodium catalyst and proposed a mechanism for the reaction. They also reported that the N_2O+CO reaction rate is several orders of magnitude lower than the rates of the $NO+CO$ and O_2+CO reactions. Cho (21) presented a kinetic analysis showing that the rate of the N_2O+CO reaction, as an intermediate reaction in the $NO+CO$ reaction system, can be two to three orders of magnitude higher than the rate of the isolated N_2O+CO reaction.

It is possible that the lack of a single rate-controlling step for all conditions is responsible for several different mechanisms having been proposed for the reduction reaction of N_2O by CO. Alternatively, the fact that a derived rate expression is consistent with the experimental data provides only a necessary but not a sufficient condition that a model is based upon the correct reaction mechanism. Very good agreement is often possible solely because rate functions of the Langmuir-Hinshelwood type are very adept at fitting data. An additional interesting observation is that, despite the similarity of the N_2O+CO and O_2+CO reaction systems, there are as yet no reports in the literature of multiplicity behavior for the N_2O+CO reaction on noble metal catalysts.

In an earlier study, Graham and Lynch (22), used the steady-state multiplicity behavior of the O_2+CO reaction over supported platinum catalyst to discriminate among several kinetic models. In this study, a similar discrimination among several kinetic models will be performed by using the experimental bifurcation behavior for the reduction of N_2O by CO over a supported platinum catalyst. The steady-state multiplicity for this reaction has been observed over the temperature range of 460-520 K. Four kinetic models are examined and it is shown that only a model based on carbon monoxide self-exclusion from the platinum catalyst is able to describe all of the observed behavior. The

9

proposed mechanism consists of several elementary steps, namely, the reversible adsorption of CO, the irreversible dissociative adsorption of N_2O to form adsorbed atomic oxygen and gaseous N_2, and the reaction of adsorbed carbon monoxide and atomic oxygen to form gaseous CO_2. A kinetic model based on this reaction mechanism and incorporating the CO self-exclusion effect is able to describe the reaction rate multiplicity with an explicit rate expression.

2.2 Experimental Equipment and Materials

The recycle reactor system used in this study has been previously used by Lynch and Wanke (23). The subsequent modifications to the feed metering and controlling system were done by Graham and Lynch (22, 24). Further modifications to the system for the purpose of this study, include computer automation and replacement of the infrared spectrophotometer by dedicated gas analyzers. The experimental equipment can be grouped into three major parts, a recycle reactor system, feed system and gas analyzers.

The recycle reactor system is shown in Figure 2.1. The recycle reactor vessel is constructed from a 2.5 cm diameter stainless steel pipe, with a total free volume of 47 cm³. The reactor contained 20 g of Englehard catalyst containing 0.5 wt% platinum supported on $\gamma-Al_2O_3$ in the form of pellets. The cylindrical pellets were approximately 3 mm by 3 mm in size, with the Pt deposited in a thin layer on the exterior.portion of the pellets. The catalyst bed was diluted with 60 g of 3 mm diameter glass beads. As a result of some of the modifications to the recycle tubing, the effective free volume of the recycle system including the reactor (without the catalyst and the glass beads), metal bellows compressor and the associated tubing was determined to be 215 cm³ from frequency response measurements similar to those described by Lynch and Walters (25).

The reactor was placed in a fluidized sand bath equipped with a resistance heater, controlled by a Barber-Coleman model 520 solid-state controller. The reactor

FLUIDIZED BED SAND-BATH

REACTOR

RECYCLE PUMP

HEATED COMPARTMENT

FEED

VENT

INFRARED GAS ANALYZERS

VIA-300
N_2O

PIR-2000
NO

PIR-2000
CO_2
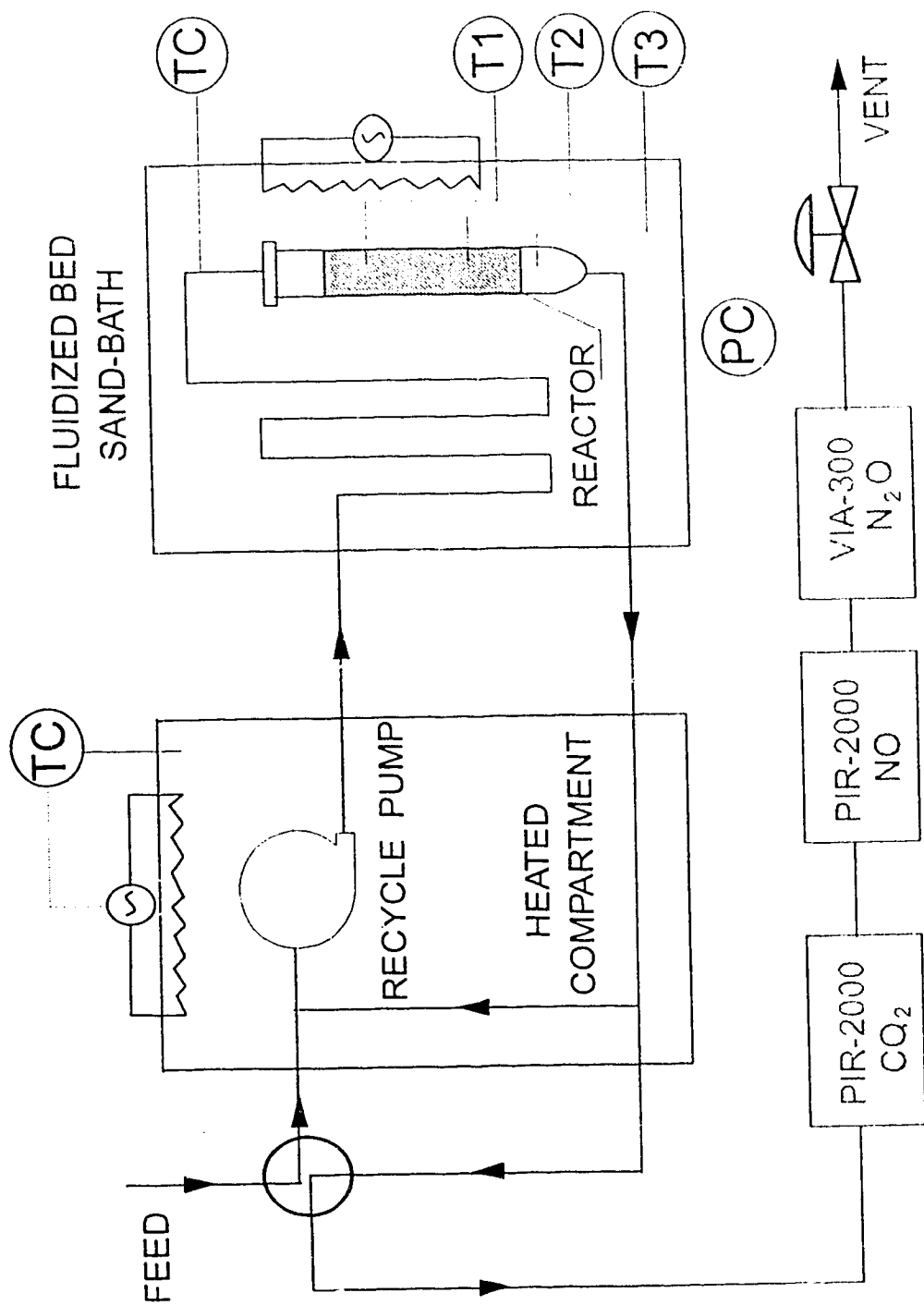
Figure 2.1 Recycle Reactor System Schematic.

11

temperatures were monitored by four type J thermocouples, two of which were inserted into the catalyst bed, one was inserted below the catalyst bed and one was inserted into the inlet tubing at the top of the rea. .or. The inlet temperature was used to control the heat input to the sand bath. The inlet consisted of approximately 1 m of 6.4 mm diameter stainless-steel tubing immersed in the sand bath. The reactor operated essentially isothermally with a maximum recorded temperature difference of 2 K across the catalyst bed. The temperature controller was able to maintain the reactor temperature within ±1 K. A Metal Bellows Corporation model MB-118 HT compressor driven by a 1 hp variable speed motor was used for gas recirculation. The motor speed could be manually set in the range of 300-2000 rpm. At the normal operating speed of 1400 rpm, the recycle flow from the pump was measured to be 500 cm^3/s. The reactor pressure was always maintained at 103 kPa and the temperatures used in this study were 461, 480, 499 and 520 K. Thus, for a feed flow of 185 cm^3(STP)/min, a recycle ratio of 85 to 98 was achieved at the reactor operating conditions. From frequency response measurements, the mixing in the reactor was found to approximate closely that of an ideal CSTR.

The recycle compressor and the recycle tubing were housed in an insulated box equipped with a resistance heater and a recirculating fan for preheating of the feed gas. The temperature in the preheat compartment was maintained at 150 °C, and was limited by the softening temperature of the teflon seals of the bellows compressor. The exit stream from the reactor was routed to gas analyzers. The reactor pressure was maintained at 103 kPa by means of a Moore Instrument Co. model 40-100 pressure regulator, located downstream of the gas analyzers. The reactor pressure was measured by a Hiese model 7108 B digital absolute pressure gauge.

The feed gas system is shown schematically in Figure 2.2. The feed composition and the flow rates were controlled by three Matheson model 8250 mass flow controllers. The mass flow controllers for CO and N_2O had a span of 100 cm^3 (STP)/min and the controller for the total flow to the reactor has a span of 500 cm^3/min. Flow rates between 15% and 85% of the span could be accurately set on these mass flow controllers. An

12
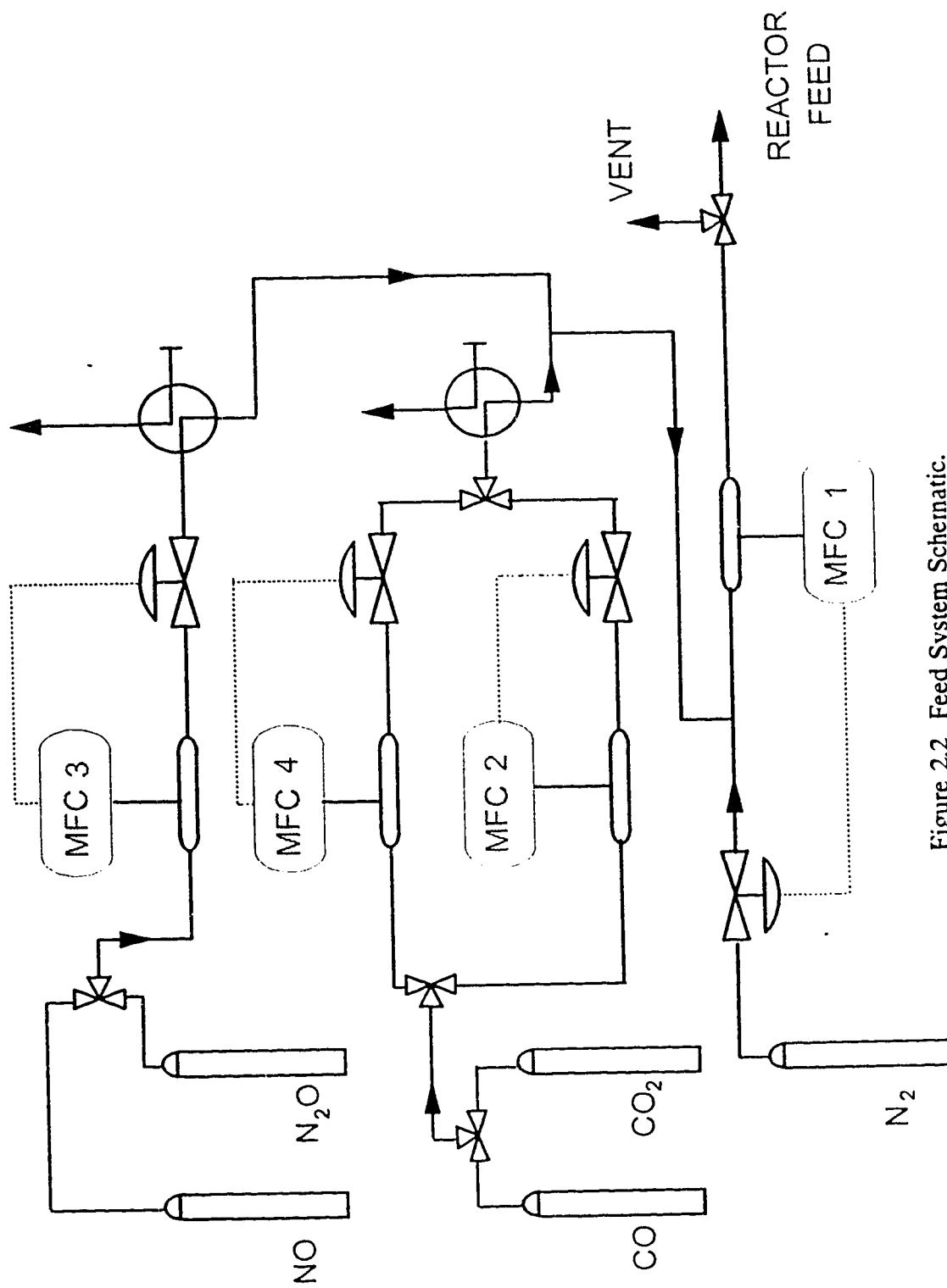
Figure 2.2 Feed System Schematic.

additional mass flow controller, Matheson model 8259, with a range of 0-30 cm³(STP)/min was installed in parallel with the CO mass flow controller and it was used for metering small flows of CO. The flow controllers were calibrated using a bubble column. The calibration charts for the mass flow controllers are shown in Appendix A. An air-actuated four-way valve, Whitey model 131 DA, was located downstream of each of the CO and N_2O mass flow controllers. The flow controllers and the valves were interfaced to an IBM-compatible microcomputer using Optomux digital/analogue conversion equipment. This equipment was also used for monitoring reactor temperatures, individual and total flow rates and the on-line gas analyzers. The gases used for this study were purchased from Linde and included gas mixtures of 2%, 5% or 10% CO in N_2; 2% or 10% N_2O in N_2 and prepurified N_2. Feed compositions were in the ranges of 0-2% N_2O and 0-2% CO, with nitrogen for the balance of the feed.

The effluent stream from the reactor was routed through two in red type gas analyzers connected in series. Horiba infrared gas analyzers PIR-2000 and VIA-300 were used for measuring CO_2 and N_2O respectively. The analyzers were calibrated at the beginning of each experiment, using N_2 for zero calibration and a gas mixture (0.982% CO_2 in N_2, 2% CO_2 in N_2, or 2% N_2O in N_2) for the span calibration.

2.3 Results

The experiments were concerned with examining the reaction rate dependence on concentration, and the steady-state rate multiplicity behavior, in the temperature range of 460-520 K. Matsuura and Kato (26) have shown that steady-state rate multiplicity occurs for heterogeneous catalytic reactions in an isothermal CSTR when the reactant concentration in the feed is such that the rate curve intersects the CSTR mass balance line at three points on a rate versus reactant concentration plot. At least one of the three states is always unstable when multiplicity occurs. This type of feed concentration multiplicity can occur even in the absence of intrinsic rate multiplicity which can be represented by hysteresis in the rate versus reactor concentration curve. Eigenberger (27) has shown that

14

intrinsic rate multiplicity can be caused by the competing chemisorption of two species upon the same active sites of a catalyst and that the rate expression has to be implicit to possess multiple solutions. The experiments described herein were aimed at studying multiplicity as described by Matsuura and Kato (26) rather than intrinsic rate multiplicity as described by Eigenberger (27). Emphasis was particularly placed on determination of the reactor feed composition at which bifurcation in steady-state CO conversion occurs. The term "bifurcation point" will be used to refer to the CO feed concentration at which the CO conversion abruptly changes from a low to a high value, or from a high to a low value.

In the first group of experiments, the reactor temperature, the total feed flow rate to the reactor and the N_2O concentration in the feed were held constant while varying the CO feed concentration during each experimental run. Sets of measurements were made at each of three different temperatures, 461, 480 and 499 K, respectively, and, at each temperature, experiments were carried out using three different N_2O concentrations, 0.4%, 0.7% and 1.2%, respectively. The results of these nine sets of experimental data are summarized in Fig. 2.3 and tabulated in Appendix B.

At the beginning of each experiment, the CO feed concentration was set to be much less than the N_2O feed concentration. The attainment of steady-state was determined by monitoring the CO_2 and N_2O concentrations in the reactor effluent stream. The CO feed concentration was then increased in steps, allowing a minimum of 3 hours at every step to reach steady-state conditions. It was observed that, while the CO conversion was 100% at low CO feed concentrations, increasing the CO concentration beyond a certain limit (high-to-low conversion bifurcation point) caused the CO conversion to drop from nearly 100% to a very low value. For example, for the right-most curve in Fig. 2.3(a) (499 K, 1.2% N_2O), the high-to-low conversion bifurcation occurred for a feed containing between 1.055% and 1.082% CO. Each experiment was then repeated starting with a feed CO concentration which was much in excess of the feed N_2O concentration (low conversion region). Stepwise decrease of the %CO in the feed
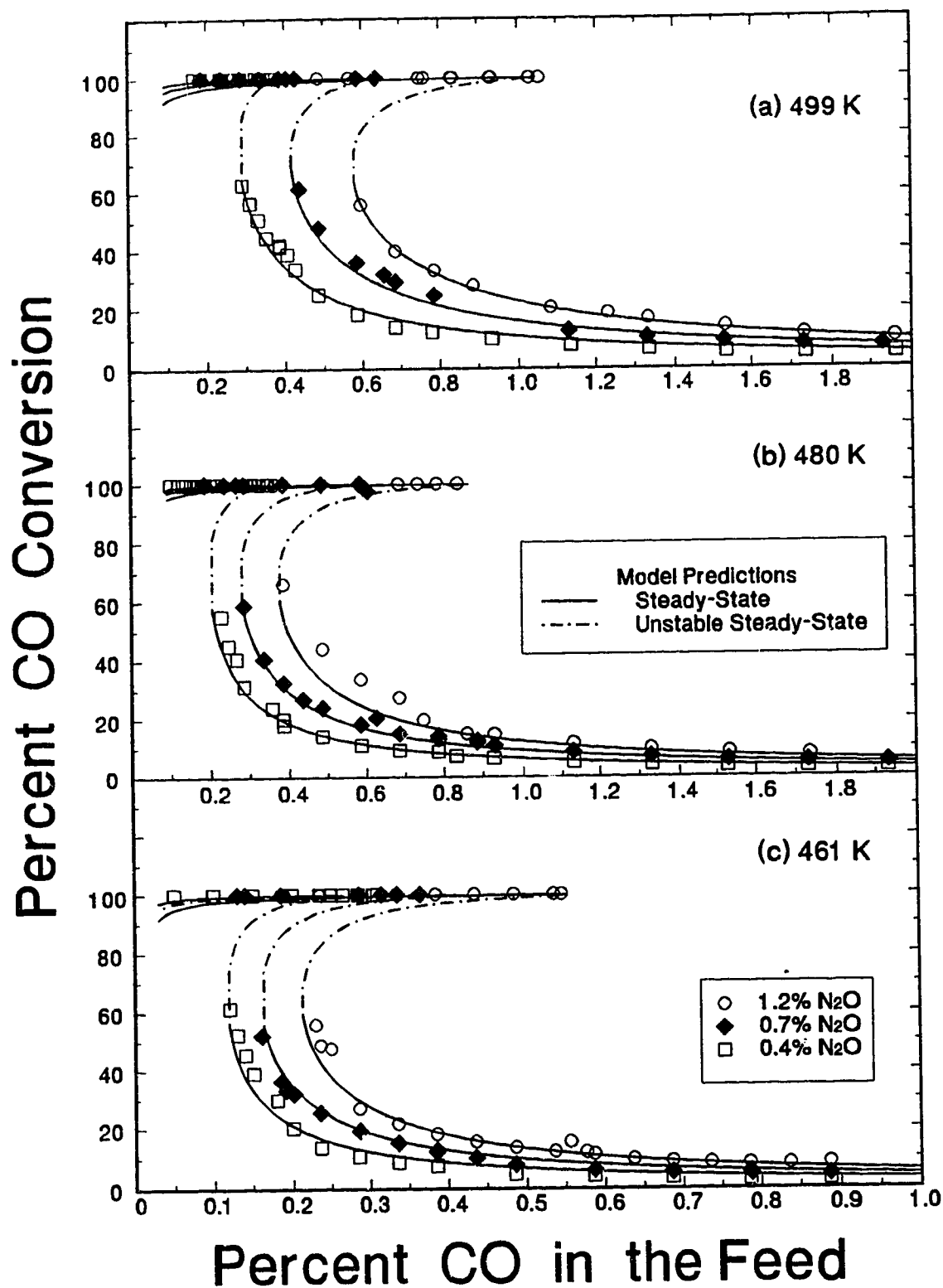
Figure 2.3 Multiplicity Behavior During the Reduction of N_2O by CO at 461-499 K.

caused the conversion to increase gradually (from nearly 10% at 1.96% CO to nearly 55% at 0.596% CO as shown by the open circles in Fig. 2.3(a). Further decrease in CO feed concentration, below the low-to-high conversion bifurcation point, caused the CO conversion to increase to 100%. In Fig. 2.3(a), the low-to-high conversion bifurcation occurred at a feed CO composition of between 0.586% and 0.596% for the experiment with 1.2% N_2O in the feed. The bifurcation points were bracketed by repeating the experiments with small step sizes in CO feed concentration, until reproducible steady-states were achieved. Operating periods of longer than 3 hours were often necessary in order to bracket a bifurcation point.

An additional three sets of experiments were carried out at 520 K by reversing the roles of CO and N_2O. For the experiments at 520 K, the N_2O concentration in the feed was varied while holding the %CO in the feed constant for each of the experimental runs. The results of three runs, with feed CO of 0.676%, 0.915% and 1.166%, respectively, are summarized in Fig. 2.4. Although Fig. 2.4 has a totally different appearance when compared to Fig. 2.3, the multiplicity behavior shown in both of the figures is similar. As can be seen from Fig. 2.4, almost 100% CO conversion was obtained for experiments with N_2O in large excess relative to CO. Decreasing the N_2O concentration below the composition corresponding to the high-to-low conversion bifurcation point caused the CO conversion to drop from 100% to a much lower value. A low CO conversion was obtained in the experiments which were started with excess CO in the feed. Increasing the N_2O in the feed led to a gradual increase in the CO conversion. Near the low-to-high conversion bifurcation point, the CO conversion increased rapidly to 100%.

The experimental locations of the bifurcation points are shown by paired sets of symbols in Fig. 2.5. The pair of an empty symbol and a dark empty symbol brackets a low-to-high conversion bifurcation point and the pair of a dark empty symbol and a filled symbol brackets a high-to-low conversion bifurcation point. The bifurcation points at 499 K are not shown in Fig. 2.5 for reasons of clarity. The low-to-high conversion bifurcation points at 499 K almost coincide with the high-to-low conversion bifurcation points at 461

17
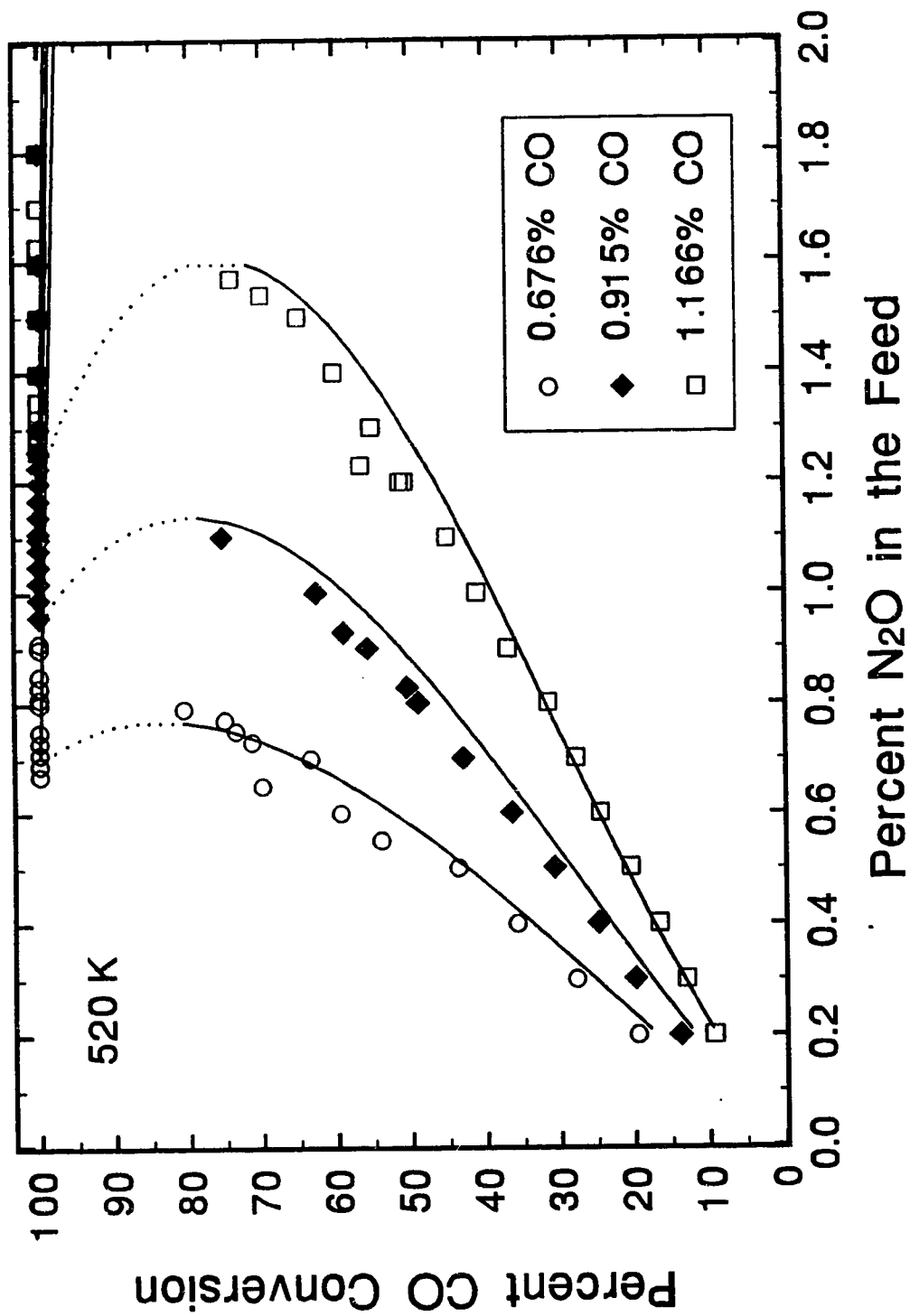
Figure 2.4 Multiplicity Behavior During the Reduction of N_2O by CO at 520 K.
(————, steady-state and ·········, unstable steady-state predicted by Mechanism 4)
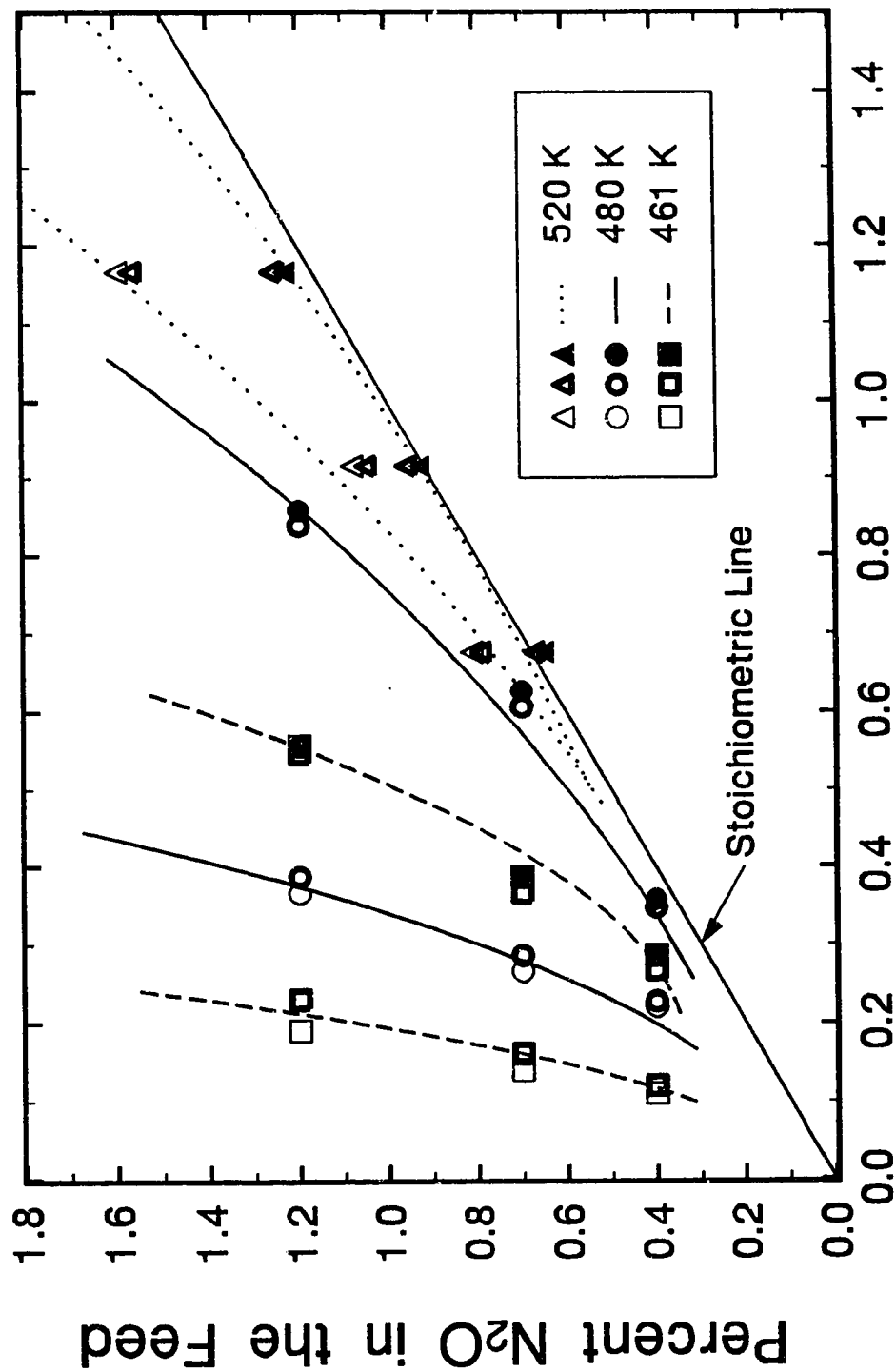
Figure 2.5 Dependence of Bifurcation Points on Temperature and Feed Composition.
(———— , ———— , ········ predictions from Mechanism 4)

61

K. The high-to-low conversion bifurcation points at 499 K lie between the two 520 K bifurcation boundaries. The multiplicity region lies within the two bifurcation boundaries. In the region to the left of the low-to-high conversion bifurcation boundary, CO conversion is almost 100%. The low conversion region lies to the right of the high-to-low conversion bifurcation boundary. It can be seen from Fig. 2.5 that the bifurcation point locations shift in the direction of higher %CO with increasing temperature and increasing %N_2O in the feed.

It is generally agreed that during N_2O reduction by CO, an adsorbed oxygen species is formed through N_2O decomposition. In addition to reaction with CO, it is possible that an oxygen desorption reaction could also be involved as a process for removal of surface oxygen. Therefore, a sensitive oxygen analyzer (Customs Sensors and Technology model 8205 - lowest range 0-2 ppm O_2) was employed to measure reactor oxygen content with a feed consisting of 1.5% N_2O in N_2 at 499 K. No change in oxygen content between the feed and effluent streams could be detected, therefore, oxygen desorption does not occur in the temperature range under consideration. In another experiment with a feed containing 2% CO in N_2, no CO_2 could be detected in the reactor effluent, therefore, reaction between two adsorbed CO molecules to form CO_2 and surface carbon does not occur at the temperatures used in this study.

To ensure that the experimental measurements represent the intrinsic kinetics of the reaction, it is necessary to determine to what extent, if any, the experimental observations have been affected by internal and external mass transfer limitations. The absence of inter-particle mass transfer effects was verified experimentally by varying the recycle flow delivered by the compressor. No effect on CO conversion was observed for a wide range of recycle flow rates. In addition, the ratio of the surface CO concentration to bulk CO concentration, calculated from a mass transfer coefficient correlation (28), was predicted to be approximately 0.995 for the experiments, which further confirms the absence of the inter-particle mass transfer resistance. The intra-particle diffusional effects were expected to be negligible because the catalyst was an egg-shell type catalyst in

which all of the platinum was deposited in the outer 10% (or less) of the volume of the pellets. Moreover, the per-pass conversion in the reactor was always less than 1%.

Intra-particle diffusional effects were also assessed by determining the value of a Thiele modulus of the form:

$$\phi_S = \frac{r_p^2(-r_{CO})}{D_{eff}C_S} \tag{2.1}$$

Satterfield (28) suggests that, for an isothermal system consisting of an irreversible reaction of a single reactant, whose kinetics can be represented by a power-law relationship, intrinsic kinetics are observed if $\Phi_S < 6$ for a zeroth-order reaction or $\Phi_S < 1$ for a first-order reaction. In addition Smith et al. (29) have shown that for a negative-order reaction, $\Phi_S < 10$ is sufficient for intrinsic kinetics to be measured. For the experimental data in the low-conversion regions of Figs 2.3 and 2.4 (negative-order kinetics with respect to CO), the calculated values of Φ_S vary from a low of 0.01 (at 461 K for 0.4% N_2O and 0.67% CO in the feed) to a high of 1.6 (at 520 K with 0.8% N_2O and 0.67% CO in the feed). Therefore, it can be said that the measurements in the low-conversion region are not affected by internal diffusion limitations. Unfortunately, the same can not be stated conclusively for the high-conversion (positive-order kinetics with almost 100% CO conversion) because it was not possible to determine the very low reactor concentrations reliably with the gas analysis equipment employed in this study. Thus, because of the possibility of diffusional effects on the high-conversion data, emphasis has been placed in the following on using the low-conversion data for discrimination among the various mechanisms and estimation of the model parameters. The high-conversion data has only been used to the extent that, when estimating parameters, an attempt has always been made to have model experimental agreement regarding the locations of the high-to-low conversion bifurcation points.

21

2.4 Models of Reaction Mechanism

The overall reaction in which CO is oxidized by N_2O involves elementary steps consisting of adsorption, desorption and surface reaction. In the temperature range of interest (<600 K), CO adsorbs reversibly on platinum (30). The adsorption and/or decomposition of N_2O on platinum and other noble metal catalysts have been studied by several authors. Lintz and Riekert (31) compared the reaction probabilities of N_2O decomposition from several studies and they concluded that the observations regarding the N_2O+CO system were quite reproducible. Alnot et al. (32) reported the dissociative adsorption of N_2O on a recrystallized platinum ribbon with the release of molecular N_2 in the temperature range 300-500 K. Takoudis and Schmidt (33) studied the kinetics of N_2O decomposition on polycrystalline Pt in the temperature range of 673-1473 K and proposed a Langmuir-Hinshelwood rate expression. In their derivation, the rate limiting step was assumed to be the decomposition of adsorbed N_2O, while adsorption-desorption equilibrium was assumed for both N_2O and O_2. They also concluded that the surface coverage of adsorbed N_2O is equal to unity at low temperature and proportional to the partial pressure of N_2O at high temperatures. However, in a later study, Schmidt et al. (34) reported that N_2O does not appear to chemisorb on platinum in UHV experiments in the temperature range of 700-1600 K.

The surface reaction between adsorbed CO and adsorbed oxygen is believed to be the main reaction for the production of CO_2 (17, 21) when CO is oxidized by N_2O. However, an Eley-Rideal type reaction between gas-phase CO and oxygen has also been suggested (20) as a route for the production of CO_2 in the overall N_2O+CO reaction.

A main consideration in proposing a reaction mechanism is that it should be able to describe the experimental multiplicity behavior. In this study, four mechanisms have been examined in an attempt to describe the experimental bifurcation and reaction rate behavior of the N_2O+CO reaction.

2.4.1 Mechanism 1

The first mechanism used to describe the rate multiplicity was a classical Langmuir-Hinshelwood type model consisting of the following elementary steps.

$$CO(g) + M \;\rightleftharpoons\; M\text{-}CO \tag{2.2}$$

$$N_2O(g) + M \;\rightarrow\; N_2(g) + M\text{-}O \tag{2.3}$$

$$M\text{-}CO + M\text{-}O \;\rightarrow\; CO_2(g) + 2M \tag{2.4}$$
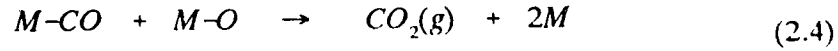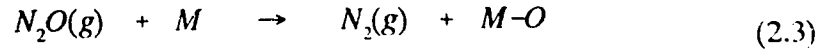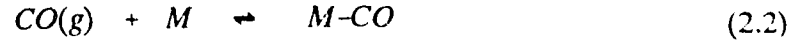
At steady-state, the mass balance equations for the adsorbed species can be written as follows, where all parameters are defined in the **Notation** section:

$$k_1 L[CO](1-\theta_{CO}-\theta_O) - k_{-1}L\theta_{CO} - k_3 L^2\theta_O\theta_{CO} = 0 \tag{2.5}$$

$$k_2 L[N_2O](1-\theta_{CO}-\theta_O) - k_3 L^2\theta_O\theta_{CO} = 0 \tag{2.6}$$

Equations (2.5) and (2.6) can be solved to express the fractional surface coverage of CO and oxygen in terms of the CO and N_2O gas-phase concentrations as given by Equations (2.7) and (2.8), respectively:

$$\theta_{CO} = \frac{K_1[CO] - (K_{21} + K_{23})[N_2O]}{1 + K_1[CO] - K_{21}[N_2O]} \tag{2.7}$$

$$\theta_O = \frac{K_{23}[N_2O]}{K_1[CO] - K_{21}[N_2O]} \tag{2.8}$$

The specific rate of CO_2 formation is given by:

$$r_{CO_2} = K_{LH} \theta_o \theta_{CO} \qquad (2.9)$$

The reactor is assumed to be an ideal CSTR, and therefore, the gas-phase species mass balances are given by the following two equations:

$$Q([CO]_o - [CO]) = WK_{LH} \theta_o \theta_{CO} \qquad (2.10)$$

$$Q([CO]_o - [CO]) = Q([N_2O]_o - [N_2O]) \qquad (2.11)$$

Equations (2.7), (2.8), (2.10) and (2.11) can be used to relate the percentage CO conversion to the reactant compositions in the reactor. Because the experimental CO conversion is known as a function of reactant concentrations, it is possible to estimate the values of the kinetic parameters so as to obtain agreement between the model and the data. An initial estimate of the parameters was obtained by forcing the model predictions to match the low-to-high conversion bifurcation point locations. The experimental data for near 100% CO conversion were not used for the initial parameter estimation, because it was not possible to determine the very low reactor concentrations reliably with the gas analysis equipment employed in this study when the CO conversion approached 100%. The final parameter values were selected to minimize the sum of squared errors in the predicted bifurcation points.

In Fig. 2.6, the CO conversion predictions from Mechanism 1 ˆˉe compared with th ˌ ˈerimental data (represented by the solid circles) at 499 K with 1.2% N_2O in the feed. The parameter values used for Fig. 2.6 are listed in Table 2.1. To generate a continuous curve, Equations (2.7),(2.8),(2.10) and (2.11) were reduced to a single, cubic equation in [N_2O] by successive substitution. The roots of the cubic equation for [N_2O] were then determined by the 'roots' function of MATLAB (35) with different values of %CO in the feed. MATLAB programs for calculation of CO conversion by various mechanisms are listed in Appendix C. The [N_2O] equation has three physically

24
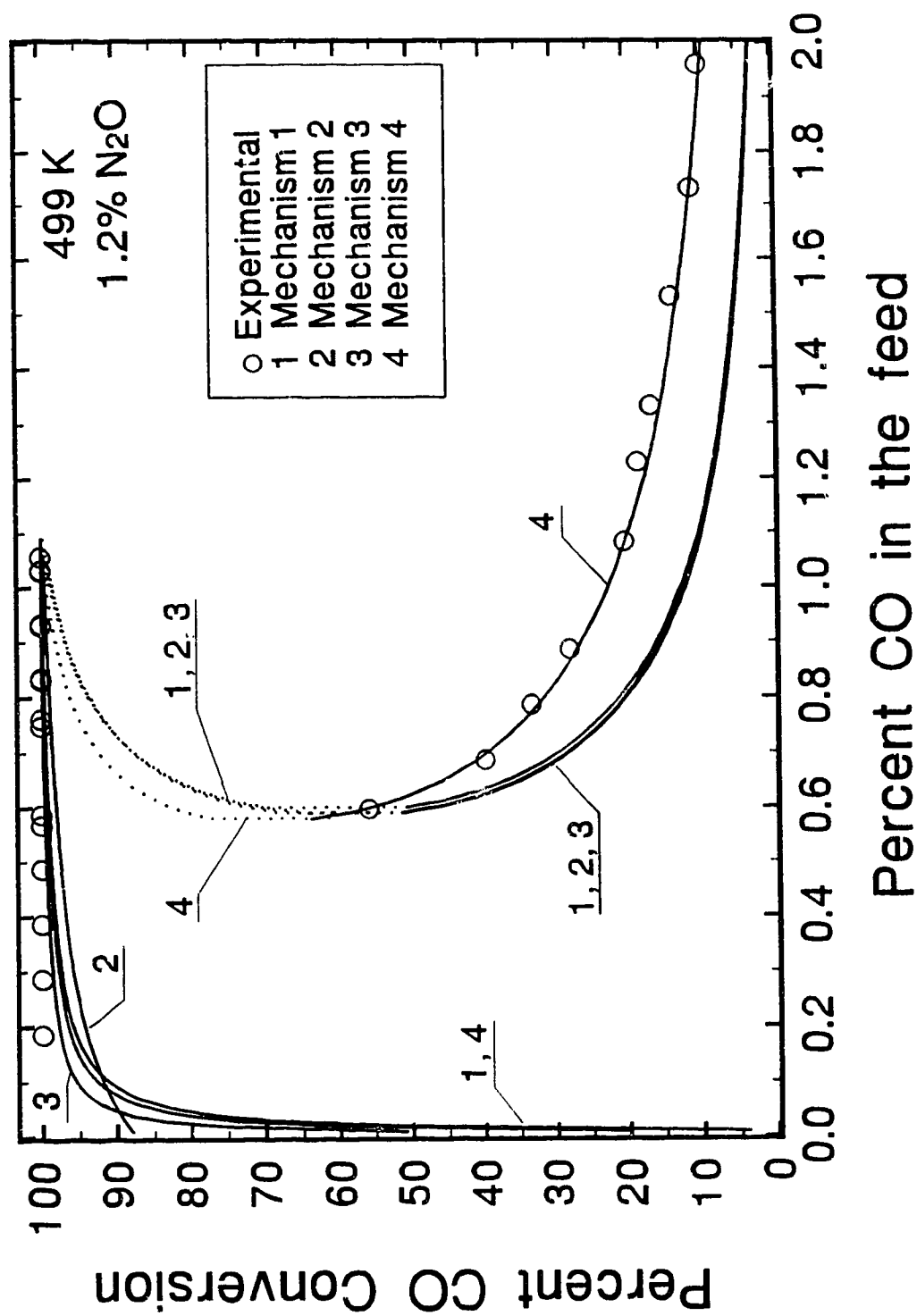
Figure 2.6 Comparison of Predictions from Mechanisms 1 to 4 to Experimental Bifurcation Points and CO Conversions.

reasonable roots in the region of multiplicity. The dotted lines in Fig. 2.6 indicate that the steady state is unstable; in the multiplicity region two of the steady states are stable and one is unstable. It can be seen from Fig. 2.6 that the predictions from Mechanism 1 match the experimental bifurcation points. However, the predicted CO conversions are somewhat less than the experimental values in the region of low CO concentrations in the feed (<0.3%CO) and very markedly less than the experimental values in the region of high CO concentrations in the feed (0.6%-2%). An attempt was made to adjust the parameter values to obtain better agreement between the experiments and the predictions, however, it was not possible to find a single set of parameter values that could describe both the experimental CO conversions as well as the bifurcation point locations.

Table 2.1

Parameter Values at 499 K for Mechanism 1 to 4

Parameter	Mechanism			
	1	2	3	4
K_1	1000	2115	605	1200
K_{21}	1.9×10^{-2}	4.5×10^{-2}		1.7×10^{-2}
K_{23}	8	39.4		8
K_{31}			1.45×10^{-3}	
K_{43}		4.9		
K_5			4.8	
K_{63}			2.4	
K_{65}			0.15	
K_{LH}	1.721×10^{-6}	3.891×10^{-7}	1.721×10^{-6}	1.371×10^{-6}
N_{co}				1.025

It is possible to increase the CO conversion on the high conversion branch (the region of low %CO in the feed) either by increasing the CO adsorption-desorption constant, K_1, or by reducing the values of the parameters K_{21} or K_{23}. However, adjusting

26

the parameters in this fashion leads to an increasing discrepancy between the predicted and the experimental locations of the high-to-low conversion bifurcation points. It is seen in Fig. 2.6 that the predicted CO conversion decreases rapidly as the CO in the feed is reduced below approximately 0.2%. This occurs because N_2O decomposition is increasingly favoured over CO adsorption as the feed %CO is reduced while holding the %N_2O constant. Thus, the oxygen surface coverage increases rapidly and inhibits CO adsorption. As the oxygen surface coverage approaches unity, the CO fractional surface coverage, and consequently the CO conversion, decreases to zero. This is at odds with the experimental data in which the CO conversion was observed to be constant at close to 100% as the feed %CO was decreased. It should be noted, however, that reliable experimental measurements were not possible for very low values of the %CO in the feed because of the previously noted analyzer limitations. The problem of oxygen saturating the surface would not occur if oxygen desorption occurs to any significant extent. However, this explanation is not applicable because, as already mentioned, the possibility of oxygen desorption was examined experimentally and ruled out.

The model predictions for the low conversion branch (high feed %CO) could be improved only slightly by increasing K_{LH} or by reducing K_1, but this can only be achieved at the expense of an increasing discrepancy in the prediction of the low-to-high conversion bifurcation point location. Specifically, both the bifurcation points shift in the direction of higher feed %CO for an increase in K_{LH} or for a decrease in K_1 or K_{23}. Both bifurcation points are relatively insensitive to changes in the value of K_{21} by as much as ±75%. The number of significant digits shown in Table 2.1 (and in subsequent tables of parameter values) does not imply that the parameters have been determined to this degree of precision. This number of significant digits is given so that others can reproduce the calculations. Changing any individual parameter can result in significant changes in the predictions but simultaneous changes to several parameters can result in equivalent predictions being produced.

27

From the preceding it is seen that the standard Langmuir-Hinshelwood type model has serious deficiencies. Although, this mechanism can describe the multiplicity behavior, it is not possible for any single set of parameter values to produce complete agreement with all of the experimental behavior (bifurcation point locations and reaction rate dependence on composition).

2.4.2 Mechanism 2

Lintz (20) proposed a mechanism for the N_2O+CO reaction over polycrystalline Pt which, in addition to the three steps of Mechanism 1, also included an Eley-Rideal (ER) reaction between gas-phase CO and adsorbed oxygen.

$$CO(g) \;+\; M\text{-}O \;\rightarrow\; CO_2(g) \;+\; M \qquad (2.12)$$
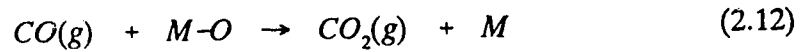
Thus, Mechanism 2 consists of the four reaction steps (2.2)-(2.4) and (2.12). The steady-state balance for the adsorbed CO is identical to Eq. (2.5), and the balance for the adsorbed oxygen is given by:

$$k_2 L[N_2O](1 \;-\; \theta_{CO} \;-\; \theta_o) \;-\; k_3 L^2\theta_o\theta_{CO} \;-\; k_4 L[CO]\theta_O \;=\; 0 \qquad (2.13)$$

The rate of CO_2 formation is given by:

$$r_{CO_2} \;=\; K_{LH}\theta_O(\theta_{CO} \;+\; K_{43}[CO]) \qquad (2.14)$$

Equations (2.5) and (2.13) cannot be solved explicitly for the fractional surface coverage of CO and oxygen in that quadratic equations are obtained for θ_{CO} and θ_O. Therefore, Eqs. (2.5), (2.10), (2.11) and (2.13) were reduced to a single tenth-order polynomial in $[N_2O]$ and solved by using the MATLAB 'roots' function. The $[N_2O]$ polynomial has three physically reasonable roots in the region of multiplicity and a single physically reasonable root elsewhere. As can be seen from Fig. 2.6, Mechanism 2 predicts near

28

100% conversion of CO at low %CO in the feed. The model parameter, K_{ji}, which is the ratio of the reaction rate constants for the ER and the surface reactions, has a value of 4.9. However, in an extensive review of CO oxidation on noble metal catalysts, Engel and Ertl (30) concluded that for CO oxidation over Pt catalysts there is a lack of evidence for the ER reaction proceeding to any significant degree. Thus, in order to predict high CO conversion in the low %CO feed region, it is necessary to have a very large value for the ER rate constant, relative to the LH rate constant, which is inconsistent with earlier studies. In addition, as seen in Fig. 2.6, the use of the ER reaction does not produce any improvement in the prediction of the low conversion branch, relative to Mechanism 1. Hence, the inclusion of an ER step cannot be used to eliminate the model-experimental discrepancies noted in Mechanism 1.

2.4.3 Mechanism 3

In the earlier two models, it has been assumed that N_2O adsorbs dissociatively on a platinum surface. However, as suggested by Takoudis and Schmidt (33), N_2O decomposition on platinum could occur via an adsorbed N_2O species as follows:

$$N_2O(g) + M \rightleftharpoons M\text{-}N_2O \qquad (2.15)$$

$$M\text{-}N_2O \rightarrow N_2(g) + M\text{-}O \qquad (2.16)$$
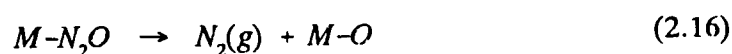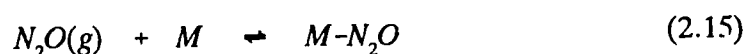
Mechanism 3 consists of four steps, namely reactions (2.2), (2.4), (2.15) and (2.16). McCabe and Wong (17) used a similar mechanism to describe N_2O reduction by CO on an alumina-supported rhodium catalyst in the temperature range of 550 to 700 K. They assumed that weakly adsorbed N_2O serves as a precursor to dissociative adsorption. The steady-state balances for the three adsorbed species yield the following equations:

$$k_1 L[CO](1 - \theta_{CO} - \theta_O - \theta_{N_2O}) - k_{-1}L\theta_{CO} - k_3 L^2\theta_O\theta_{CO} = 0 \quad (2.17)$$

$$k_5 L[N_2O](1 - \theta_{CO} - \theta_O - \theta_{N_2O}) - k_{-5}L\theta_{N_2O} - k_6 L\theta_{N_2O} = 0 \quad (2.18)$$

$$k_6 L\theta_{N_2O} - k_3 L^2\theta_O\theta_{CO} = 0 \quad (2.19)$$

Equations (2.17)-(2.19) can be rearranged to produce explicit expressions for the fractional surface coverage of CO, oxygen and N_2O, namely:

$$\theta_{CO} = \frac{K_1(1 + K_{65})[CO] - K_5 K_{63}(1 + K_{31})[N_2O]}{(1 + K_{65})(K_1[CO] + 1) + K_5(1 - K_{31}K_{63})[N_2O]} \quad (2.20)$$

$$\theta_O = \frac{K_5 K_{63}[N_2O]}{(1 + K_{65})K_1[CO] - K_5 K_{31}K_{63}[N_2O]} \quad (2.21)$$

$$\theta_{N_2O} = \frac{\theta_{CO}\theta_O}{K_{63}} \quad (2.22)$$

The rate of CO_2 formation is given by Eq. (2.9). Unfortunately, as shown in Fig. 2.6, the CO conversion predictions from Mechanism 3 are very similar to those from Mechanism 1. This was found to occur for all sets of parameter values examined provided that model-experimental agreement concerning the location of the bifurcation points was required. Thus, the existence of an adsorbed N_2O surface species cannot resolve the model-experimental discrepancies noted in Mechanism 1.

2.4.4 Mechanism 4

As shown in the preceding, for feed CO in the range of 0.6%-2%, all three of the models predict CO conversions which are much less than the experimental observations.

Therefore it can be concluded that the classical Langmuir-Hinshelwood-Hougen-Watson (LHHW) type mechanisms which were examined cannot describe the overall reaction behavior. In a study of the O_2+CO reaction, Graham and Lynch (22) encountered similar problems with the classical LHHW mechanisms. They found that, in order to obtain model-experimental agreement, it was necessary to invoke a CO self-exclusion effect, which proposes that an adsorbed CO molecule excludes other CO molecules from an area equivalent to N_{CO} surface Pt atoms, where N_{CO} is slightly greater than unity. The experimental evidence for this effect is provided by the studies of Freel (36), Dorling and Moss (37) and Yao et al. (38) who have shown that the fractional saturation coverage of the adsorbed CO on small particle size (<5nm) supported platinum is less than unity. Based on these studies, the CO self-exclusion factor, N_{CO}, has a value in the range of 1.0 to 1.25 corresponding to a CO fractional saturation coverage of 0.8 to 1.0 on a highly dispersed catalyst.

The CO self-exclusion effect does not add any additional steps to a reaction mechanism, instead it modifies the mathematical form of the rate expression for CO adsorption. Graham and Lynch (22) showed that the rate of CO adsorption with the CO self-exclusion effect is given by

$$r_{CO,ads} = k_1 L[CO](1 - \theta_{co} - \theta_o)\frac{(1 - N_{co}\theta_{co})}{(1 - \theta_{co})} \qquad (2.23)$$

In a classical Langmuir-Hinshelwood model (e.g. Mechanism 1) $N_{CO}=1$ which results in Eq. (2.23) becoming identical to the CO-adsorption term used in Eq. (2.5). Mechanism 4 consists of the same elementary steps as Mechanism 1, except that the CO self-exclusion effect has been added. For reactions (2.2) to (2.4) the steady-state balance for adsorbed oxygen is given by Eq. (2.6). However, due to the CO self-exclusion effect, the steady-state balance for adsorbed CO is modified to become:

$$k_1 L[CO](1 - \theta_{CO} - \theta_O)\frac{(1 - N_{CO}\theta_{CO})}{(1 - \theta_{CO})} - k_{-1}L\theta_{CO} - k_3 L^2\theta_{CO}\theta_O = 0 \quad (2.24)$$

Equations (2.6) and (2.24) can be solved explicitly for θ_{CO} and θ_O yielding:

$$\theta_{CO} = \frac{K_1[CO] - (K_{21} + K_{23})[N_2O]}{1 + N_{CO}K_1[CO] - K_{21}[N_2O]} \quad (2.25)$$

$$\theta_O = \frac{K_{23}[N_2O](1 + (N_{CO} - 1)K_1[CO] + K_{23}[N_2O])}{(K_1[CO] - K_{21}[N_2O]) + K_{23}[N_2O](N_{CO}K_1[CO] - K_{21}[N_2O])} \quad (2.26)$$

It is seen that Eqs. (2.25) and (2.26) reduce to Eqs. (2.7) and (2.8), respectively, for a value of N_{CO} equal to unity. The rate of formation of CO_2 is given by Eq. (2.9). It can be seen from Fig. 2.6 that the predictions from Mechanism 4 are markedly improved relative to the first three mechanisms. The CO conversion predictions for the low-conversion branch exactly match the experimental results while maintaining agreement with the location of the bifurcation points, something which was not possible for the first three mechanisms. Of course, the CO self-exclusion effect does not significantly affect the conversion predictions in the high-conversion region because in this region the CO fractional surface coverage is very low.

A further test for Mechanism 4 is to determine if the predictive ability of the model is not limited to just the data in Fig. 2.6, but instead can be used over a wide range of experimental conditions. As shown in Figs. 2.3 and 2.4, for a constant value of the CO self-exclusion factor, $N_{CO}=1.025$, the conversion predictions of Mechanism 4 are in excellent agreement with the twelve sets of experimental data which span wide ranges of temperature and feed compositions. In addition, as shown in Fig. 2.5, Mechanism 4 is also able to describe the composition and temperature dependence of the bifurcation

32

boundaries.

As given in Table 2.2, different sets of values of the rate parameters (K_1, K_{21}, K_{23}, K_{LH}) are, of course, needed for each of the four different temperatures used in the experiments. However, from Fig. 2.7 it is seen that an Arrhenius-type temperature dependency holds for each of the four rate parameters. It should be noted that, because several of the rate parameters are ratios of rate constants, it is possible to have both positive and negative slopes. Thus, except for K_{LH}, the values of E/R given in Table 2.2 are grouped terms which are not true activation energies. Assuming that CO adsorption is non-activated, the activation energy for CO desorption, E_{-1}, is calculated from E_1/R to be 41.0 kJ/mol. Similarly, the activation energy of the surface reaction between adsorbed CO and oxygen species, E_3, is calculated from E_{LH}/R to be 74.5 kJ/mol. The activation energy for the N$_2$O dissociation reaction, E_2, can be calculated from either the sum of E_{23}/R and E_{LH}/R or by subtracting E_1/R from E_{21}/R. The former approach yields a value of 91.2 kJ/mol while the latter gives a value of 92.7 kJ/mol. It is seen that both approaches give similar results, with the average value of E_2 being 92 kJ/mol.

Table 2.2

Temperature Dependence of Parameters for Mechanism 4

Parameter	461 K	480 K	499 K	520 K	E/R
K_1	2550	1725	1200	750	-4,931
K_{21}	0.8	1.35	2.2	3.7	6,215
K_{23}	5.4	6.6	8.0	8.8	2,029
K_{LH}	1.652×10^{-7}	3.579×10^{-7}	6.538×10^{-7}	15.5×10^{-7}	8,951
N_{CO}	1.025	1.025	1.025	1.025	

The above values of activation energies obtained from estimating the parameters
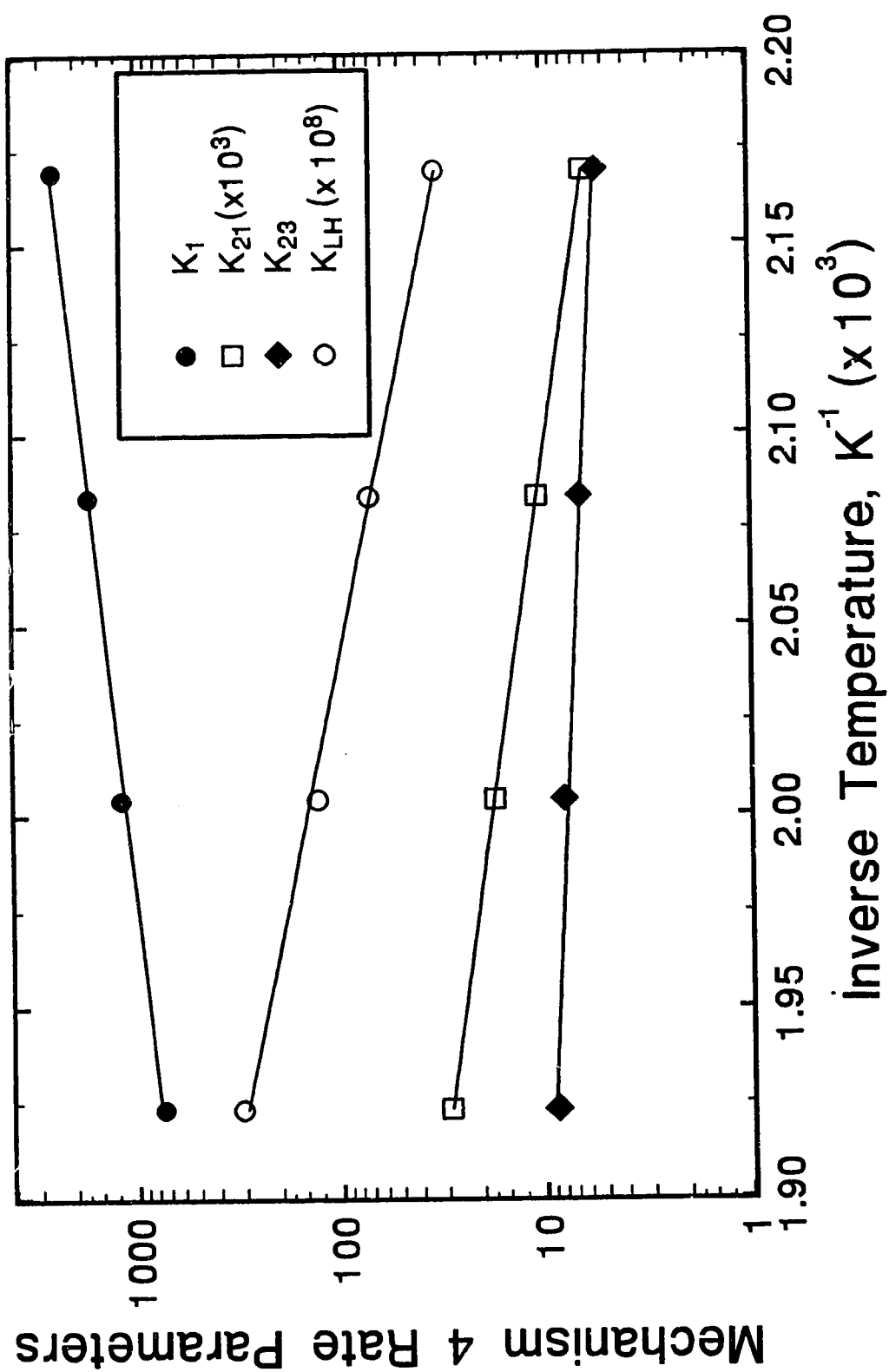
Figure 2.7 Arrhenius-Type Plot of Parameters for Mechanism 4.

for Mechanism 4 can be compared with the values obtained from other studies. Mechanism 4 predicts that the CO fractional surface coverage is close to its saturation value of $1/N_{CO}$ in the region of high %CO in the feed (the low conversion region) and drops sharply to a very low value ($\theta_{CO} < 0.1$) when the feed %CO is decreased below the low-to-high bifurcation point (the high conversion region). The apparently low value (41 kJ/mol) of the CO desorption activation energy, E_{-1}, which is needed to describe the experimental data can be attributed to the existence of a CO saturated surface when the CO conversion is low. Ertl et al. (39), using a combination of TPD, LEED and work function measurements, reported that the activation energy of CO on Pt(111) declined with CO surface coverage. They reported that the activation energy of adsorption decreases linearly from 138 kJ/mol at $\theta_{CO} \approx 0$ to 113 kJ/mol at $\theta_{CO} = 0.5$, at which point a sharp decrease to 92 kJ/mol occurred, followed by a rapid decrease in E_{-1} for $\theta_{CO} > 0.6$. They derived an isosteric heat of adsorption of approximately 54 kJ/mol at $\theta_{CO} = 0.7$ from LEED data. Seebauer et al. (40) also reported a similar coverage dependence for the heat of adsorption of CO on Pt(111) using laser induced thermal desorption measurements. They found that the heat of adsorption of 134 kJ/mol at low coverage declined rapidly with surface coverage to a low value of 42 kJ/mol at near saturation coverage of $\theta_{CO} > 0.6$. The pre-exponential factor of CO desorption was also reported to have a low value of 3×10^7 for a CO saturated surface. The value of E_{-1} of 41.0 kJ/mol used in this study to describe the experimental data is thus seen to be close to the values of 54 kJ/mol and 42 kJ/mol reported by Ertl et al. (39) and Seebauer et al. (40), respectively, for CO saturated Pt(111) surface.

In an extensive review of CO oxidation over platinum, Engel and Ertl (30) reported that the value of the activation energy of the LH reaction between adsorbed CO and the adsorbed oxygen, E_3, has been found from several studies to be in the range of 33 to 96 kJ/mol, although they contend that a value of 33 kJ/mol may not be justified. Several studies (22, 24, 41-43) have used values of 40 to 80 kJ/mol for E_3 to describe CO oxidation on platinum. The value of E_3=74.5 kJ/mol used in this study falls in the range of values from these other studies. Although the value of the activation energy for

gaseous N_2O dissociation on Pt, E_2, is not readily available from prior experimental studies reported in the literature, values of 146 kJ/mol (33) and 75 kJ/mol (17) have been used in modelling studies for the activation energy of dissociation of adsorbed N_2O as compared with a value of E_2=92 kJ/mol used in this study.

As shown in Figs. 2.3 to 2.6, Mechanism 4 can provide an excellent description of the experimental observations. However, some caution must still be exercised because it is found that several quite dissimilar sets of values can all produce similar descriptions of the data. This difficulty has previously been noticed by Graham and Lynch (22) and can be resolved by using both dynamic and steady-state data when estimating parameter values. Thus, while it was not possible to change an individual parameter value from that given in Table 2.2 without producing an increased model-experimental discrepancy, it nevertheless is possible to maintain excellent model-experimental agreement by making simultaneous adjustments to several (or all) of the parameter values. This is shown in Table 2.3 where three alternative sets of parameter values (Cases I to III) are given which produce very similar (essentially identical) model predictions compared to the base case parameters. As can be seen from Table 2.3, the low values of CO desorption energy, E_{-1}, and pre-exponential factor, k_1^o, are consistent with the model prediction of the surface being saturated with CO in the low CO conversion region. The model predictions for the high conversion region (with low %CO in the feed) show that the fractional coverage is less than 0.4.

To examine further the effect of the coverage dependence of the CO desorption activation on the model predictions, a step change in the CO adsorption and desorption rate constants was incorporated in the model. With this modification the CO conversion was calculated using the parameters listed in Table 2.2 while decreasing the feed %CO, and a step change in the values of E_{-1}, k_1^o and S_{CO} to 134 kJ/mol, 10^{15} s^{-1} and 0.6, respectively was made at the low-to-high bifurcation point. The predictions from the modified model are shown in Fig 2.8. As can be seen from Fig. 2.8, the CO conversions in the high conversion region are in excellent agreement with the experimental data.

36
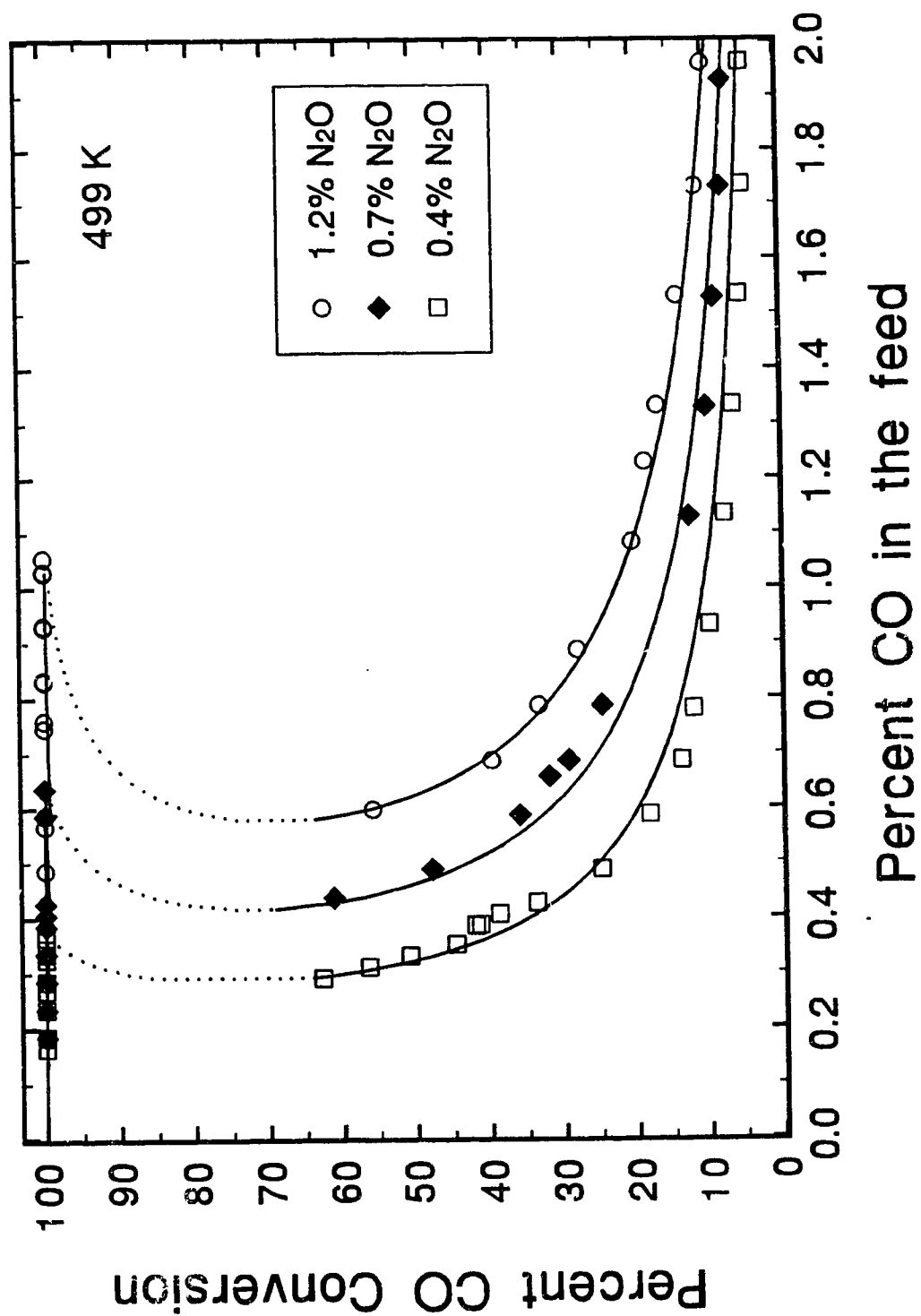
Figure 2.8 Predictions from Mechanism 4 at 499 K with Coverage Dependent Adsorption and Desorption Rate Constants.

However, because the parameters K_1 and K_{23} are coverage dependent, the rate expression is not explicit in terms of gas phase concentrations of CO and N_2O.

Table 2.3

Sets of Kinetic Parameters for Mechanism 4 which Give Similar Predictions

Parameter	Base Case	Case I	Case II	Case III
K_1 (499 K)	1200	900	1100	960
K_{21} (499 K)	0.0173	0.012	0.0123	0.0123
K_{23} (499 K)	8	7.85	4	8
K_{LH} (499 K)	1.308×10^{-6}	1.3×10^{-6}	1.0×10^{-6}	1.27×10^{-6}
N_{co}	1.025	1.02	1.0275	1.025
E_{-1}	41.0	49.8	39.7	51.0
E_2	92.0	79.1	85.8	78.7
E_3	74.5	65.7	75.3	65.7
k_{-1}^o	305×10^6	1.513×10^7	8.16×10^5	1.847×10^7
k_2^o	02×10^9	2.013×10^8	4.669×10^8	1.857×10^8
k_3^o	4.684×10^{11}	5.185×10^{10}	4.381×10^{11}	5.093×10^{10}
S_{co}	0.01	0.01	0.01	0.01

The rate of CO_2 formation is given by Eq. (2.9), where the fractional surface coverage for CO and oxygen are given by Eqs. (2.25) and (2.26), respectively. The rate expressions can be simplified in the unique low-conversion and the unique high-conversion regions. In the unique low-conversion region of Fig. 2.6, the numerical predictions indicate that the fractional surface coverage of CO is close to its saturation value which is equal to the inverse of N_{CO}. The same conclusion can be drawn from Eq. (2.25) by considering that in the unique low-conversion (high feed %CO) region, $K_1[CO]$ is orders of magnitude greater than $K_{21}[N_2O]$ and $K_{23}[N_2O]$ and therefore Eq. (2.25) can be simplified as follows:

38

$$\theta_{co} = \frac{1}{N_{co}} \qquad (2.27)$$

Similarly Eq. (2.26) can be simplified as follows:

$$\theta_o = \frac{K_{23}[N_2O](1 + (N_{co} - 1)K_1[CO] + K_{23}[N_2O])}{K_1[CO](1 + K_{23}N_{co}[N_2O])} \qquad (2.28)$$

Therefore the rate of reaction for the unique low-conversion steady-state can be determined by the following equation:

$$r_{co_2} = \frac{K_{Lf}K_{23}[N_2O](1 + (N_{co} - 1)K_1[CO] + K_3[N_2O])}{N_{co}K_1[CO](1 + K_{23}N_{co}[N_2O])} \qquad (2.29)$$

In the unique high-conversion region, the numerical predictions from Mechanism 4 show that the surface is essentially covered with oxygen. Therefore, the CO self-exclusion effect does not affect the predictions in the unique high-conversion region. This can readily be seen from Fig. 2.6, where the CO conversion predictions by Mechanism 4 are very similar to those from Mechanism 1 for low feed %CO. Therefore, the rate function for the unique high-conversion region can be simplified by assuming a value of unity for the CO self-exclusion factor $N_{CO}=1$. The rate expression, Eq.(2.9), combined with Eqs. (2.25) and (2.26) with $N_{CO}=1$, yield:

$$r_{co_2} = \frac{K_{Lf}K_{23}[N_2O](K_1[CO] + (K_{2i} - K_{23})[N_2O])}{(K_1[CO] - K_{21}[N_2O])(1 + K_1[CO] - K_{21}[N_2O])} \qquad (2.30)$$

Equation (2.30), essentially, predicts the rate of CO_2 formation by Mechanism 1, where CO self-exclusion effect was not considered. The rate predictions from Eqs. (2.29) and (2.30) are compared with the experimental data at 499 K with 1.2% N_2O in the

39

Fig. 2.9. It can be seen from Fig. 2.9 that Eqs. (29) and (30) describe the rate behavior in the unique low-conversion and the unique high-conversion region, respectively and they also describe the rate behavior for a part of the multiplicity region.

Notwithstanding the concern with respect to uniqueness of the values of the model parameters, of the four mechanisms examined herein, Mechanism 4 incorporating the CO self-exclusion effect is the only kinetic model that predicts CO conversions for the low-conversion steady-states which are as high as the values obtained experimentally. However, as seen in Fig. 2.3, in the region of high CO conversion a slight discrepancy is apparent between the model and the experimental data, particularly for very low values of %CO in the feed. As shown in Fig. 2.8, it is possible to predict CO conversions near 100% for low %CO in the feed by incorporating coverage dependent CO adsorption and desorption rate constants. It is also possible to predict CO conversions near 100% for low %CO in the feed by incorporating an oxygen self-exclusion effect in the model. Herz and Marin (44) have proposed the existence of such an effect in an attempt to describe the steady-state oxidation of CO by O_2 on supported platinum catalysts. In their model, the oxygen self-exclusion effect was very large, with oxygen being excluded from up to one-half of the surface ($N_O=2$). Lynch (45) used a similar oxygen self-exclusion effect to describe CO oxidation on a Pt catalyst during forced composition cycling. Incorporation of this effect into Mechanism 4 (or Mechanism 1) would modify the balance equation for surface oxygen as follows:

$$k_2 L [N_2 O](1 - \theta_{co} - \theta_o)\frac{(1 - N_o\theta_o)}{(1 - \theta_o)} - k_3 L^2 \theta_o \theta_{co} = 0 \qquad (2.31)$$

However, if the oxygen self-exclusion effect is incorporated in Mechanism 4, it is not possible to obtain an explicit rate expression in terms of CO and N_2O concentrations. Therefore, the effect of oxygen self-exclusion was tested on Mechanism 1. From the solution of Eqs. (2.5), (2.10), (2.11) and (2.31) it is found that CO conversions of near 100% can be obtained for feed CO of less than 0.2% by using a very small value of

40
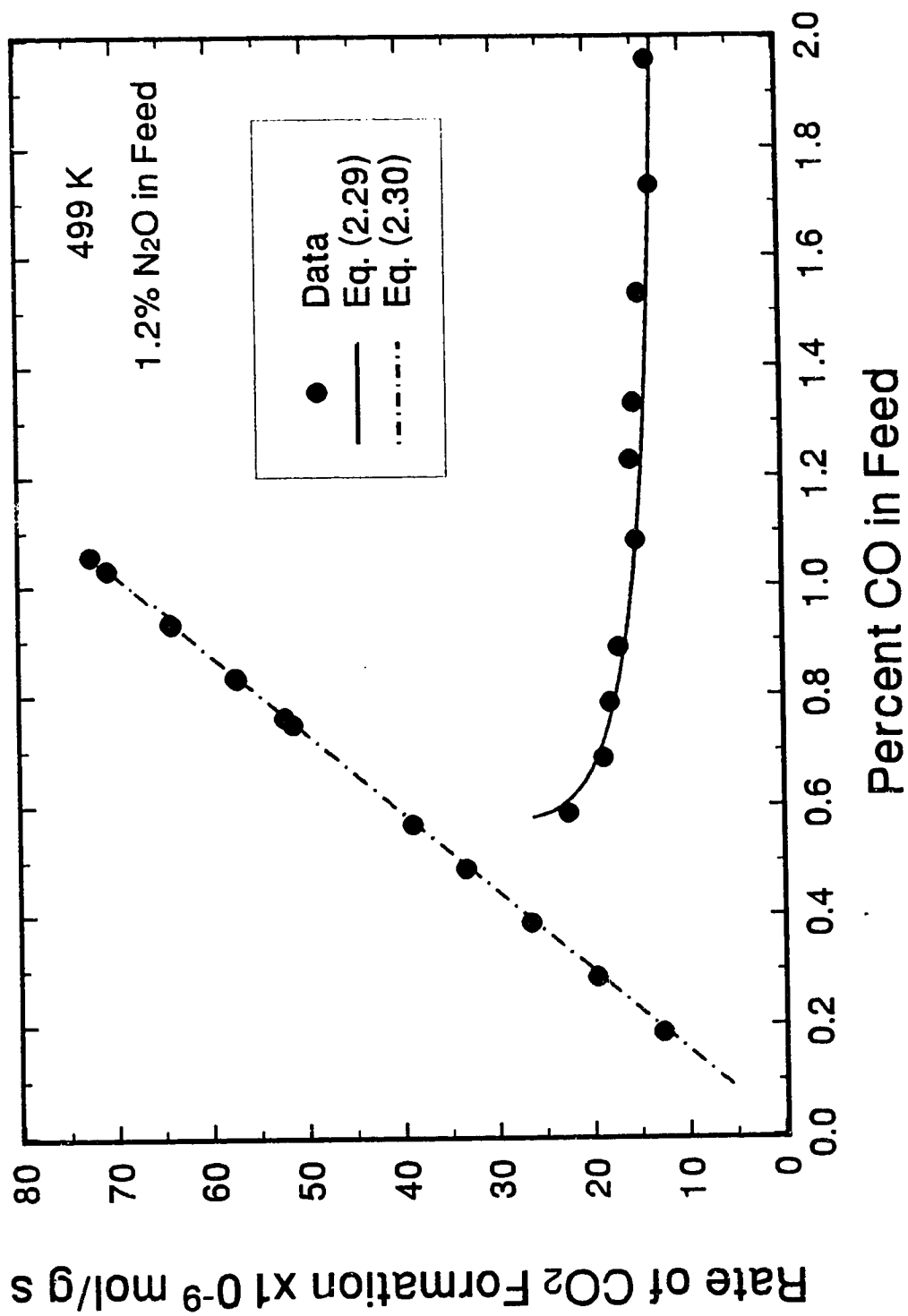
Figure 2.9 Reaction Rates in the Unique Steady-State Regions.

41

$N_0 = 1.008$ for the oxygen self-exclusion factor.

2.5 Conclusions

The N_2O+CO reaction over an alumina-supported platinum catalyst exhibits steady-state multiplicity in the temperature range of 461-520 K. To our knowledge, this is the first report of steady-state multiplicity for the N_2O+CO reaction. The effects of temperature and feed composition on the bifurcation boundaries have been determined. The bifurcation points shift in the direction of increasing feed %CO with increasing temperature and increasing %N_2O in the feed.

All of the four kinetic models examined in this study were able to predict the existence of reaction rate multiplicity. However, for high values of %CO in the feed, only a model based on a CO self-exclusion effect could quantitatively describe both the bifurcation point locations as well as predict CO conversions which were in agreement with the experimental observations. The same conclusion has previously been reached by Graham and Lynch (22) from an examination of several possible mechanisms for the O_2+CO reaction on a supported platinum catalyst. The proposed mechanism consists of several elementary steps, namely, the reversible adsorption of CO, the irreversible dissociative adsorption of N_2O to form gaseous N_2 and adsorbed atomic oxygen, and the surface reaction between adsorbed CO and adsorbed atomic oxygen to form gaseous CO_2. The CO self-exclusion effect allows N_2O to adsorb on a CO saturated-surface and, therefore, the predicted CO conversions for high %CO in the feed are as high as the experimental values. Complete model-experimental agreement in the high-conversion region required either incorporation of a coverage dependent CO desorption activation energy or the use of an oxygen self-exclusion effect.

2.6 Notation

a total Pt surface area of supported catalyst, 9.4 m^2

Symbol	Definition
$[CO]$	reactor CO concentration, mol/m^3
$[CO]_o$	feed CO concentration, mol/m^3
C_S	gas-phase concentration of CO at catalyst particle surface, mol/cm^3
D_{eff}	effective diffusion coefficient for CO into an alumina pellet with a BET surface area of 109 m^2/g and an average pore size of 3 nm, 2.3×10^{-3} cm^2/s at 499 K
$E_{1,H}/R$	slope of Arrhenius-type ⸺ model parameter $K_{1,H}$, K
E_1/R	slope of Arrhenius-type cu⸺or model parameter K_1, K
E_{-1}	activation energy for CO desorption, kJ/mol
E_2	activation energy for N_2O dissociation, kJ/mol
E_3	activation energy for surface reaction, kJ/mol
E_{21}/R	slope of Arrhenius-type curve for model parameter K_{21}, K
E_{23}/R	slope Arrhenius-type curve for model parameter K_{23}, K
k_1	CO adsorption rate constant, $6.87 S_{CO}\sqrt{T}/L$ $m^3/mol \cdot s$
k_{-1}	CO desorption rate constant, $k^o_{-1}exp(-E_{-1}/RT)$, s^{-1}
k^o_{-1}	CO desorption pre-exponential factor, s^{-1}
k_2	N_2O dissociation rate constant, $k^o_2exp(-E_2/RT)$, $m^3/mol \cdot s$
k^o_2	N_2O dissociation pre-exponential factor, $m^3/s \cdot mol$
k_3	surface reaction rate constant, $k^o_3exp(-E_3/RT)$, $m^2/mol \cdot s$
k_4	Eley-Rideal reaction rate constant, $m^3/mol \cdot s$
k_5	N_2O adsorption rate constant, $m^3/mol \cdot s$
k_{-5}	N_2O desorption rate constant, s^{-1}
k_6	N_2O-M dissociation rate constant, s^{-1}
K_1	ratio of CO adsorption to desorption rate constants, (k_1/k_{-1}), m^3/mol
K_{21}	ratio of N_2O decomposition to CO desorption rate constants, (k_2/k_{-1}), m^3/mol
K_{23}	ratio of N_2O decomposition to surface reaction rate constants, (k_2/k_3L), m^3/mol
K_{31}	ratio of surface reaction to CO desorption rate constants, (k_3L/k_{-1})

K_{43}	ratio of Eley-Rideal to surface reaction rate constants, (k_4/k_3L), m^3/mol
K_5	ratio of N_2O adsorption to desorption rate constants, (k_5/k_{-5}), m^3/mol
K_{63}	ratio of N_2O-M decomposition to surface reaction rate constants, (k_6/k_3L), m^3/mol
K_{65}	ratio of N_2O-M decomposition to N_2O desorption rate constants, (k_6/k_{-5})
K_{III}	surface reaction rate parameter, (ak_3L^2/W), mol/g·s
L	adsorption capacity of platinum surface, 2×10^{-5} mol/m^2
M	vacant site on platinum surface
M-CO	adsorbed CO species on catalyst surface
M-N_2O	adsorbed N_2O species on catalyst surface
M-O	adsorbed oxygen species on catalyst surface
N_{CO}	CO self-exclusion factor
N_O	oxygen self-exclusion factor
$[N_2O]$	reactor N_2O concentration, mol/m^3
$[N_2O]_o$	feed N_2O concentration, mol/m^3
Q	total feed flow rate to the reactor at reactor conditions, $1.11 \times 10^{-8}T$, m^3/s
$-r_{CO}$	observed reaction rate based on catalyst volume, mol/s·cm^3
$-r_{CO,ads}$	rate of CO adsorption, mol/m^2·s
r_{CO_2}	rate of CO_2 formation, mol/g·s
r_p	radius of catalyst particle, (3×volume/surface area), 0.15 cm
S_{CO}	CO sticking probability on platinum catalyst surface
T	reactor temperature, K
W	mass of catalyst, 20 g

Greek Letters

θ_{CO}	fractional CO surface coverage
θ_{N_2O}	fractional N_2O surface coverage
θ_O	fractional oxygen surface coverage

ϕ_s Thiele modulus

2.7 References

1. Bolten, H., Hahn, T., LeRoux, J. and Lintz, H.G., *Surf. Sci.* 164, L529-L532 (1985).

2. Schwartz, S.B. and Schmidt, L.D., *Surf. Sci.* 206, 169-186 (1988).

3. Adlhoch, W. and Lintz, H.G., *Z. Phys. Chem., Neue Folge* 103, 207-211 (1976).

4. Adlhoch, W., Lintz, H.ᶜ and Weisker, T., *Surf. Sci.* 103, 576-585 (1981).

5. Lesley, M.W. and Schmidt, L.D., *Surf. Sci.* 155, 215-240 (1985).

6. Schwartz, S.B. and Schmidt, L.D., *Surf. Sci.* 183, L269-L277 (1987).

7. Schüth, F. and Wicke, E., in "Instationary Processes and Dynamic Experimental

   Methods in Catalysis, Electrochemistry and Corrosion", (G. Sandstede and G. Kreysa,

   Eds.), Dechema Monogr. Vol. 120, p. 429-441 (1989).

8. Imbhil, R., Fink, Th. and Krisher, K., *J. Chem. Phys.* 96, 6236-6248 (1992).

9. Shelef, M. and Otto, K., *J. Catal.* 10, 408-412 (1968).

10. Lambert, R.M. and Comrie, C.M., *Surf. Sci.* 46, 61-80 (1974).

11. Adlhoch, W. and Lintz, H.G., *Surf. Sci.* 78, 58-68 (1978).

12. Lorimer, D. and Bell, A.T., *J. Catal.* 59, 223-238 (1979).

13. Hecker, W.C. and Bell, A.T., *J. Catal.* 84, 200-215 (1983).

14. Klein, R.L., Schwartz, S. and Schmidt, L.D., *J. Phys. Chem.* 89, 4908-4914 (1985).

15. Lim, K.J., Löffler, D.G. and Boudart, M., *J. Catal.* 100, 158-168 (1986).

16. Cho, B.K., Shanks, B.H. and Bailey, J.E., *J. Catal.* 115, 486-499 (1989).

17. McCabe, R.W. and Wong, C., *J. Catal.* 121, 422-431 (1990).

18. Kudo, A., Steinberg, M., Bard. A.J., Cameron, A., Fox, M.A., Mallouk, T.E., Webber, S.E. and White, J.M., *J. Catal.* **125**, 565-567 (1990).

19. Adlhoch, W., Kohler, R. and Lintz, H.G., *Z. Phys. Chem., Neue Folge* **120**, 111-118 (1980).

20. Lintz, H.G., *Surf. Sci.* **108**, L486-L489 (1981).

21. Cho, B.K., *J. Catal.* **138**, 255-266 (1992).

22. Graham, W.R.C. and Lynch, D.T., *AIChE J.* **33**, 792-800 (1987).

23. Lynch, D.T. and Wanke, S.E., *J. Catal.* **88**, 333-344 (1984).

24. Graham, W.R.C. and Lynch, D.T., *AIChE J.* **36**, 1796-1806 (1990).

25. Lynch, D.T. and Walters, N.P., *Chem. Eng. Sci.* **45**, 1089-1096 (1990).

26. Matsuura, T. and Kato, M., *Chem. Eng. Sci.* **22**, 171-184 (1967).

27. Eigenberger, G., *Chem. Eng. Sci.* **33**, 1255-1261 (1978).

28. Satterfield, C.N., "Heterogeneous Catalysis in Practice", p. 349, McGraw-Hill, New York (1980).

29. Smith, T.G., Zahradnik, J and Carberry, J.J., *Chem. Eng. Sci.* **30**, 763-767 (1975).

30. Engel, T. and Ertl, G., *Adv. in Catal.* **28**, 1-78 (1979).

31. Lintz, H.G. and Riekert, L., *J. Catal.* **88**, 244-245 (1984).

32. Alnot, M., Cassuto, A., Fussy, J. and Pentenero, A., *Jpn. J. Appl. Phys.*, Suppl. 2, Part 2, 79-84 (1974).

33. Takoudis, C.G. and Schmidt, L.D., *J. Catal.* **80**, 274-279 (1983).

34. Schmidt, L.D., Hansenberg, D., Schwartz, S. and Papapolymerou, G.A., in "Catalyst Characterization Science - Surface and Solid State Chemistry", ACS Symposium

Series 288, (M.L. Deviney and J.L. Gland, Eds.), p. 177-184 (1985).

35. The Math Works Inc., "The Student Edition of MATLAB - for MS-DOS Personal Computers", p. 394, Prentice-Hall, Engelwood Cliff, NJ (1992).

36. Freel, J., *J. Catal.* **25**, 149-160 (1972).

37. Dorling, T.A. and Moss, R.L., *J. Catal.* **7**, 378-385, (1967).

38. Yao, H.C., Sieg, M. and Plummer, H.K., *J. Catal.* **59**, 365-374 (1979).

39. Ertl, G., Neumann, M. and Streit, K.M, *Surf. Sci.* **64**, 393-410 (1977).

40. Seebauer, E.G., Kong, A.C.F. and Schmidt, L.D., *Surf. Sci.* **176**, 134-156 (1986).

41. Lynch, D.T., Emig, G. and Wanke, S.E., *J. Catal.* **97**, 456-468 (1986).

42. Kurtanjek, Ž. and Froment, G.F., *Chem. Eng. Sci.* **40**, 3189-3201 (1991).

43. Sales, B.C., Turner, J.E. and Maple, M.B., *Surf. Sci.* **114**, 381-394 (1982).

44. Herz, R.K. and Marin, S.P., *J. Catal.* **65**, 281-296 (1980).

45. Lynch, D.T., *Can. J. Chem. Eng.* **62**, 691-698 (1984).

3. N₂O REDUCTION BY CO:

FORCED COMPOSITION CYCLING **

3.1 Introduction

The reduction of nitrous oxide (N_2O) by carbon monoxide (CO) over noble metal catalysts is an important reaction during the reduction of nitric oxide by carbon monoxide in automobile catalytic converters (1-3). In an earlier study (4), described in Chapter 2, the steady-state multiplicity behavior of the N_2O+CO reaction over an alumina-supported Pt catalyst was used in discriminating among several rival mechanisms. Four kinetic models were examined and it was found that only a model based on CO self-exclusion from the platinum catalyst was able to describe all of the observed behavior. However, several dissimilar sets of values of kinetic parameters produced similar model predictions, which were all in excellent agreement with the experimental data. To resolve such questions concerning kinetic models, a variety of transient response techniques have been employed. Kobayashi (5) used step changes in the feed concentration of CO and N_2O to study the N_2O+CO reaction over a silver catalyst. From the transient response curves of CO_2 and N_2 it was possible to distinguish between the three Hougen-Watson type kinetic models which gave similar predictions for the steady-state experiments.

Graham and Lynch (6) used the experimental bifurcation behavior of the $CO+O_2$ reaction over a supported Pt catalyst to discriminate among several rival mechanisms. However, the proposed kinetic model based on a CO self-exclusion effect could not describe the complex reaction dynamics such as chaos and self-sustained oscillations. In a subsequent study (7), based on a transient response technique involving periodic

---

cycling of the feed composition, a kinetic model was proposed that could describe all of the observed complex behavior of the CO+O$_2$ reaction including steady-state multiplicity, self-sustained oscillations and rate-enhancement during feed composition cycling.

In an extensive review of the periodic operation of catalytic reactors, Bailey (8) showed that the cyclic operation of catalytic reactors can lead to large improvements in reaction rate, selectivity, or both. In addition, periodic operation can be used to gain insight into the underlying reaction mechanism. The technique of square-wave cycling has been used to study both the oxidation of CO over noble metal catalysts (7, 9-17) as well as the NO+CO reaction (1, 3). Several of these studies (9-12) reported significant increases in the time-average reaction rate of the CO+O$_2$ reaction which could not be described by a Langmuir-Hinshelwood type reaction mechanism. Lynch (13, 14) used the forced composition cycling technique to explain the resonant behavior of the CO oxidation reaction over a supported Pt catalyst. Other studies (16, 17) have used the forced cycling technique combined with infrared spectroscopy to study the underlying mechanism of CO oxidation over supported noble metal catalysts. Cho et al. (1) studied the reduction of NO by CO over a supported Rh catalyst during symmetric and asymmetric feed cycling experiments. They reported the formation of N$_2$O as an important step during the CO+NO reaction. Muraki and Fujitani (3) studied the effect of cycle period on N$_2$O selectivity for the NO+CO reaction over a supported Pt catalyst using cycled feeds. Graham and Lynch (7) used the technique of variable phase cycling of the feed composition to study the reaction dynamics of CO oxidation over an alumina supported Pt catalyst. They observed that variation of the phase angle between the oxygen and the CO feed cycles led to an increase in time-average conversion over and above that which occurs for the out-of-phase feed cycling. The phase angle between the two feed cycles was thus identified as an important parameter in maximizing the conversion.

The technique of variable phasing of inputs during forced composition cycling was used in this study of the N$_2$O+CO reaction. It is found that a time-average CO

49

conversion as high as five times the steady-state conversion can be achieved using variable-phase, forced feed cycling. The model described in Chapter 2 is found to be incapable of describing all of the observed dynamic data. This model is further improved by incorporating an additional feature, namely the adsorbate induced Pt surface-phase transition (7, 18) which leads to a consistent explanation of the observed dynamic behavior as well as the steady-state multiplicity behavior described in Chapter 2.

3. 2 Methods

The experiments were carried out using a recycle reactor system containing 20 g of 0.5 wt% Pt/Al_2O_3 catalyst supplied by Engelhard. The experimental equipment and the catalyst have been previously described in Chapter 2. From an earlier investigation (7) on a batch of a similar catalyst, the specific surface areas of the platinum catalyst and the alumina support were estimated to be 0.47 m^2/g and 104.6 m^2/g, respectively, with the CO_2 adsorption capacity of the alumina support, L_s, assumed to be 1.2×10^{-6} mol/m^2. The reactor pressure, temperature and the total feed flow to the reactor were always maintained at 103 kPa, 499 K and 185 $cm^3(STP)/min.$, respectively. The recycle ratio at the reactor operating conditions was estimated to be 90 from the measurement of the recycle pump flow. Under these conditions, as discussed previously in Chapter 2, it has been found that the mixing in the recycle reactor closely approximates that of an ideal CSTR.

The gases used in this study were purchased from Linde and included gas mixtures of 4.99% or 10% CO in N_2, 10.01% N_2O in N_2 and prepurified N_2. The feed compositions were in the ranges of 0-2.4% N_2O and 0-2.4% CO, with nitrogen for the balance of feed.

Four-way valves, located downstream of the mass flow controllers on the feed lines for CO and N_2O (Fig. 2.2), were used to generate square-wave composition cycles as described by Graham and Lynch (7, 18) The time-averaged feed composition was

maintained at 1.2% N_2O and 1.2% CO for all of the experiments in this study. This was achieved by setting the desired flow-rates of CO and N_2O through the mass flow controllers and sequer   switching the downstream four-way valves between the 'vent' position and the 'feed sition for each half cycle as shown in Fig. 3.1. The square-wave cycling of the CO and N_2O feed compositions did not affect the total feed flow rate to the recycle reactor, which was always maintained at 185 cm^3 (STP)/min. by regulating the flow of make-up nitrogen. Therefore, the recycle ratio was always maintained at approximately 90 (ideal CSTR behav   ), during the feed composition cycling.

At the start of every experim   , following purging of the reactor with nitrogen, N_2O was always introduced into the reactor before CO was admitted, and therefore, the N_2O feed cycle has a 'phase lead' over the CO feed cycle. The N_2O phase lead is expressed in terms of degrees considering a complete feed cycle to contain 360 degrees, as shown in Fig. 3.1, where feed cycling with N_2O phase leads of 90, 180 and 270 degrees are illustrated. The valve switching sequence and the cycle times could be controlled independently by digital signals from a microcomputer. Therefore, it was possible to achieve any cycle time and N_2O phase lead with the experimental equipment. The frequency of cycling is defined as the inverse of the cycle period. The cycling frequencies used in this study were in the range of 0.1 to 20 mHz.

A comparison of the steady-state operation with the cyclic operation (with feed composition cycling) of the reactor is presented on a phase-plane diagram in Fig. 3.2. As explained previously in Chapter 2, the multiplicity region lies in between the two bifurcation boundaries represented by the paired circle symbols. The region of unique high conversion steady-state lies to the left of the multiplicity region and the unique low-conversion steady-state occurs in the region to the right of the multiplicity region. For the steady-state operation (with non-cycled feed), the feed composition will always be stoichiometric with 1.2% N_2O and 1.2% CO, as shown by a diamond symbol in Fig. 3.2. As can be seen from Fig. 3.2, the steady-state operation leads to low-conversion. When the valves are cycled such that the N_2O phase lead is 0° or 360° (in-phase cycling), the
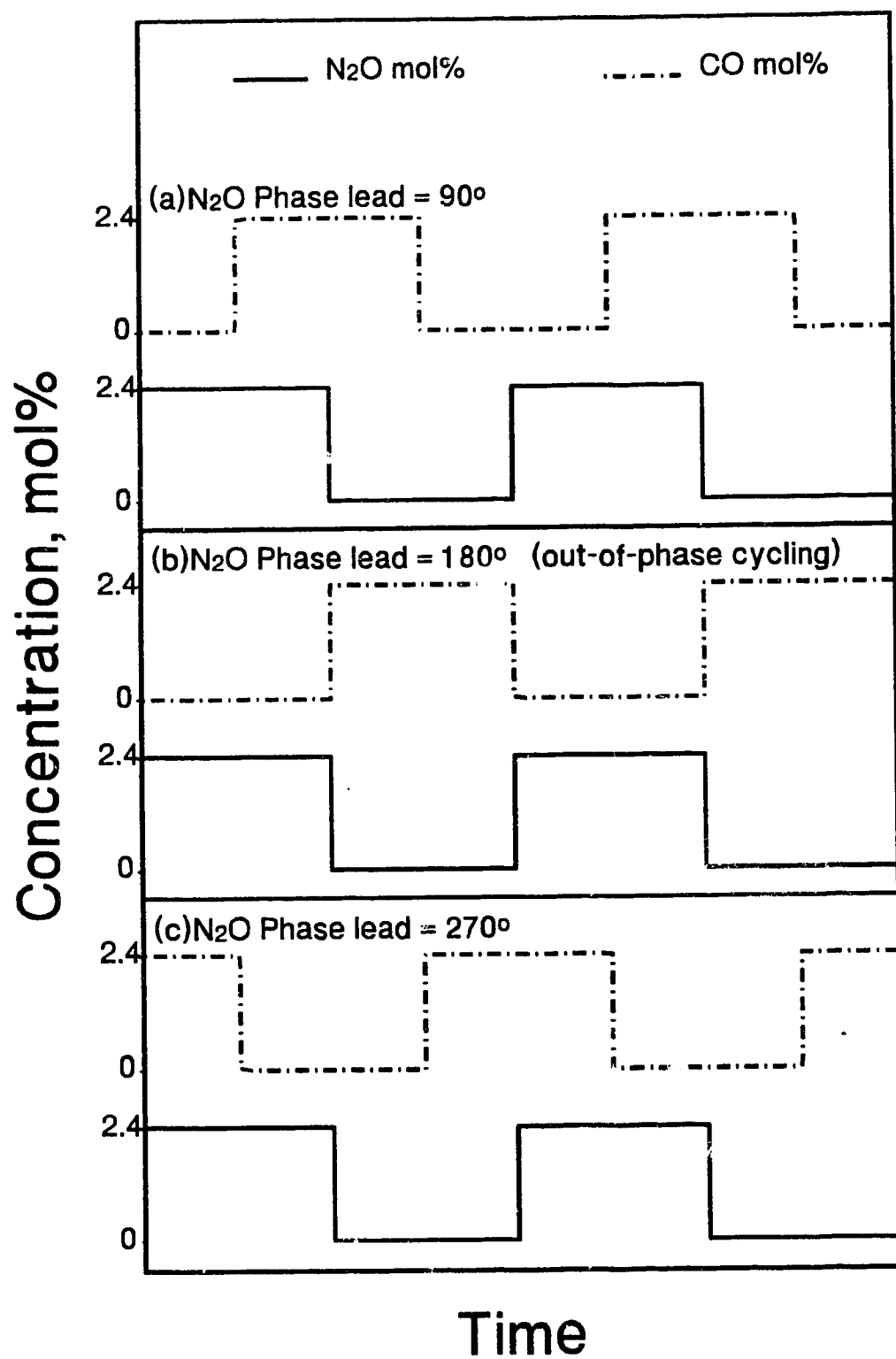
Figure 3.1 Feed Cycling Strategies
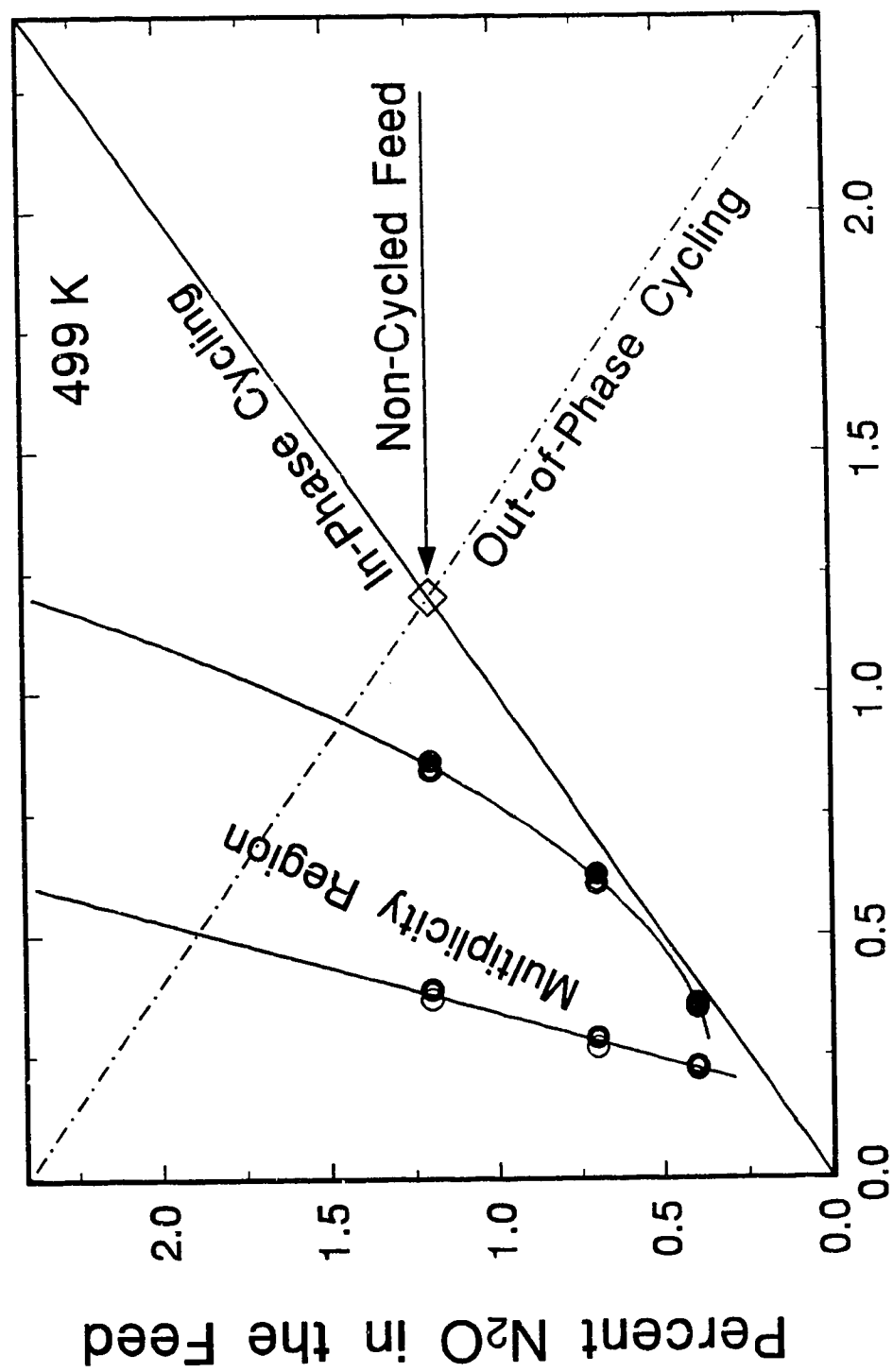
Figure 3.2 Comparison of Steady-State and Cyclic Operations

feed composition varies between (0% N_2O, 0% CO) and (2.4% N_2O, 2.4% CO) corresponding to the two end points of the solid-line diagonal. The gas-phase composition in the reactor, for in-phase cycling, is likely to be in the lower right triangle (to the right of the solid line diagonal). Therefore, the time-average conversion for the in-phase cycling will be low, as can be readily seen from Fig. 3.2. However, for the out-of-phase cycling (N_2O phase lead of 180°), the feed composition varies between the two points on the dashed-line diagonal, namely, (2.4% N_2O, 0% CO) and (0% N_2O and 2.4% CO). Therefore, the gas-phase composition in the reactor will be in the region to the left of the dashed-line diagonal, which also includes a part of the high-conversion region. Therefore, the time-average conversion during out-of-phase feed cycling will be higher than the steady-state conversion. Out of the three modes of reactor operation examined in Fig. 3.2, only the out-of-phase cycling leads to improvement in CO conversion. The effect of other values of the N_2O phase leads as well as the cycling frequencies can not be readily seen from Fig. 3.2 and these are discussed later in the chapter with respect to the experimental results.

The reactor CO_2 and N_2O concentrations were measured by Horiba infrared gas analyzers model PIR-2000 and VIA-300, respectively. The analyzers were calibrated at the beginning of each experiment using a gas mixture (2.04% CO_2 in N_2 and 2% N_2O in N_2), for the span calibration and N_2 for the zero calibration. The attainment of cycle invariance (steady-state cycling) was determined by monitoring the reactor CO_2 and N_2O responses. In general, 10 to 30 cycles were used for each experiment. A total of 306 experiments were carried out with different combinations of the cycling frequencies and the N_2O phase lead.

3.3 Results

Experiments involving feed composition cycling were carried out under isothermal conditions (499 K) with a constant total flow to the reactor so that the results could be directly compared with the results of the steady-state experiments from the earlier study

54

(4). The steady-state CO conversion at 499 K is summarized in Fig. 3.3, as a function of the feed composition. The arrows in Fig. 3.3(a) indicate the bifurcation from high-to-low and low-to-high conversion steady-states during the step-wise increase or decrease of the feed CO, respectively, when the feed N_2O is held constant at 1.2%. It can be seen from Fig. 3.3(a) that a feed composition of 1.2% CO and 1.2% N_2O is in the unique low-conversion region to the right of the multiplicity region. The steady-state CO conversion under these conditions was 20%.

In the first set of experiments, the CO and N_2O feed cycles were out-of-phase with each other, with an N_2O phase lead of 180 degrees. Therefore, the feed concentration alternated between 0% CO and 2.4% N_2O for the first half-cycle to 2.4% CO and 0% N_2O for the second half-cycle. The CO_2 response and the time-average CO conversions were determined for the out-of-phase cycling over a frequency range of 0.7 to 20 mHz. In the second part of the study, the effect of N_2O phase leads of 90 degrees and 270 degrees, respectively, on the time-average CO conversion was studied over a frequency range of 0.1 to 20 mHz. In the third part of the study, the experiments were carried out at a fixed cycling frequency and the effect of N_2O phase lead on the time-average CO conversion was studied. The experiments were repeated for five different cycling frequencies.

3.3.1 Out-of-phase cycling

The dynamic CO_2 response during out-of-phase cycling is shown by the dashed lines in Fig 3.4. At a low cycling frequency of 0.77 mHz (Fig. 3.4(a)), the CO_2 concentration increased slowly after the N_2O was switched on. At the beginning of the N_2O half-cycle, the catalyst surface is saturated with adsorbed CO from the previous CO half-cycle and gas-phase CO concentration is very close to 2.4%. Due to the lack of empty sites for N_2O dissociation, the surface reaction does not proceed to any appreciable extent. This observation is also consistent with the experimental finding that a unique low conversion steady-state was obtained for high feed CO concentrations (Fig.
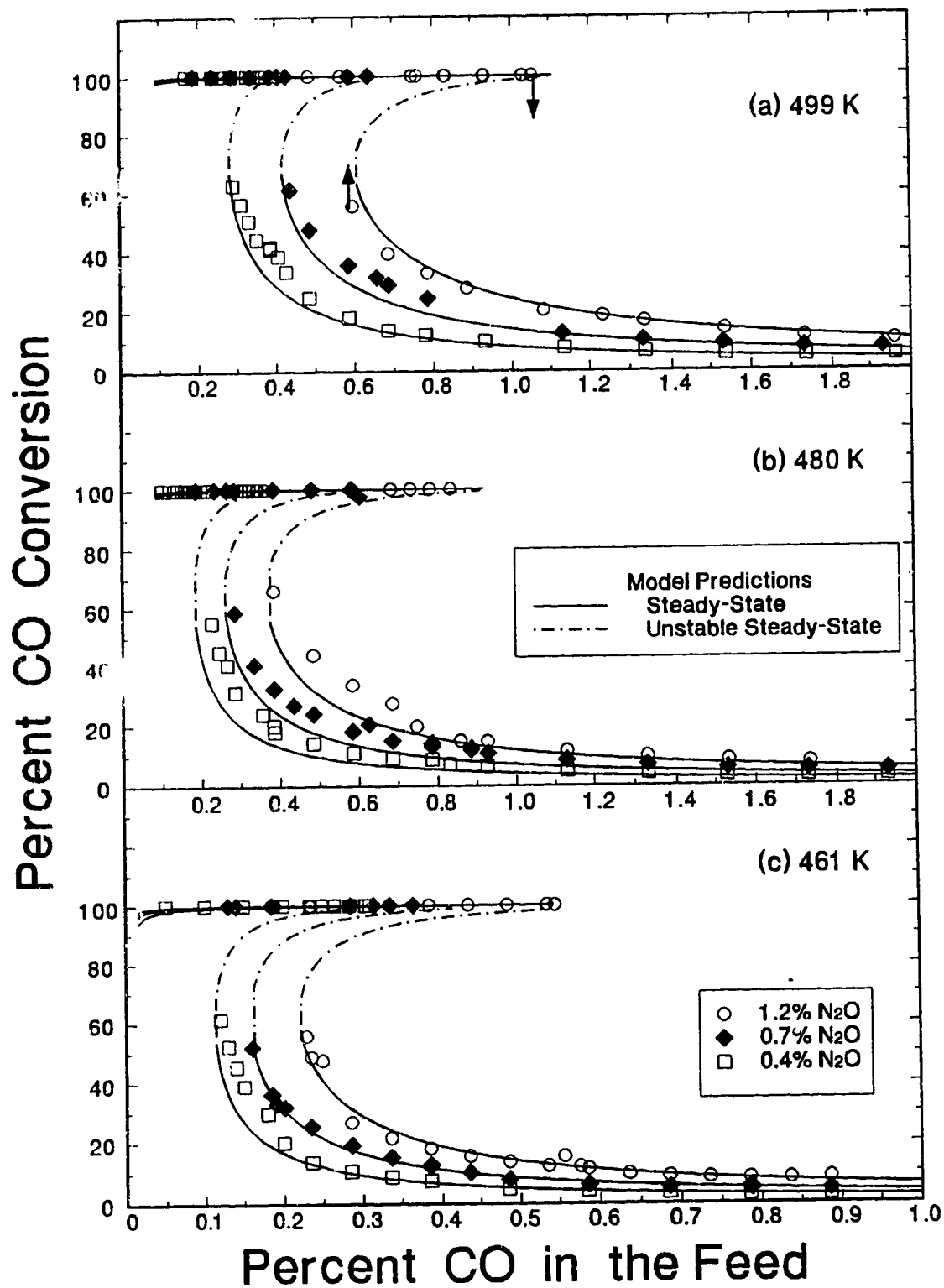
Figure 3.3 Multiplicity Behavior During the Reduction of N_2O by CO at 461 - 520 K and Predictions of Pt Surface-Phase Transition Model
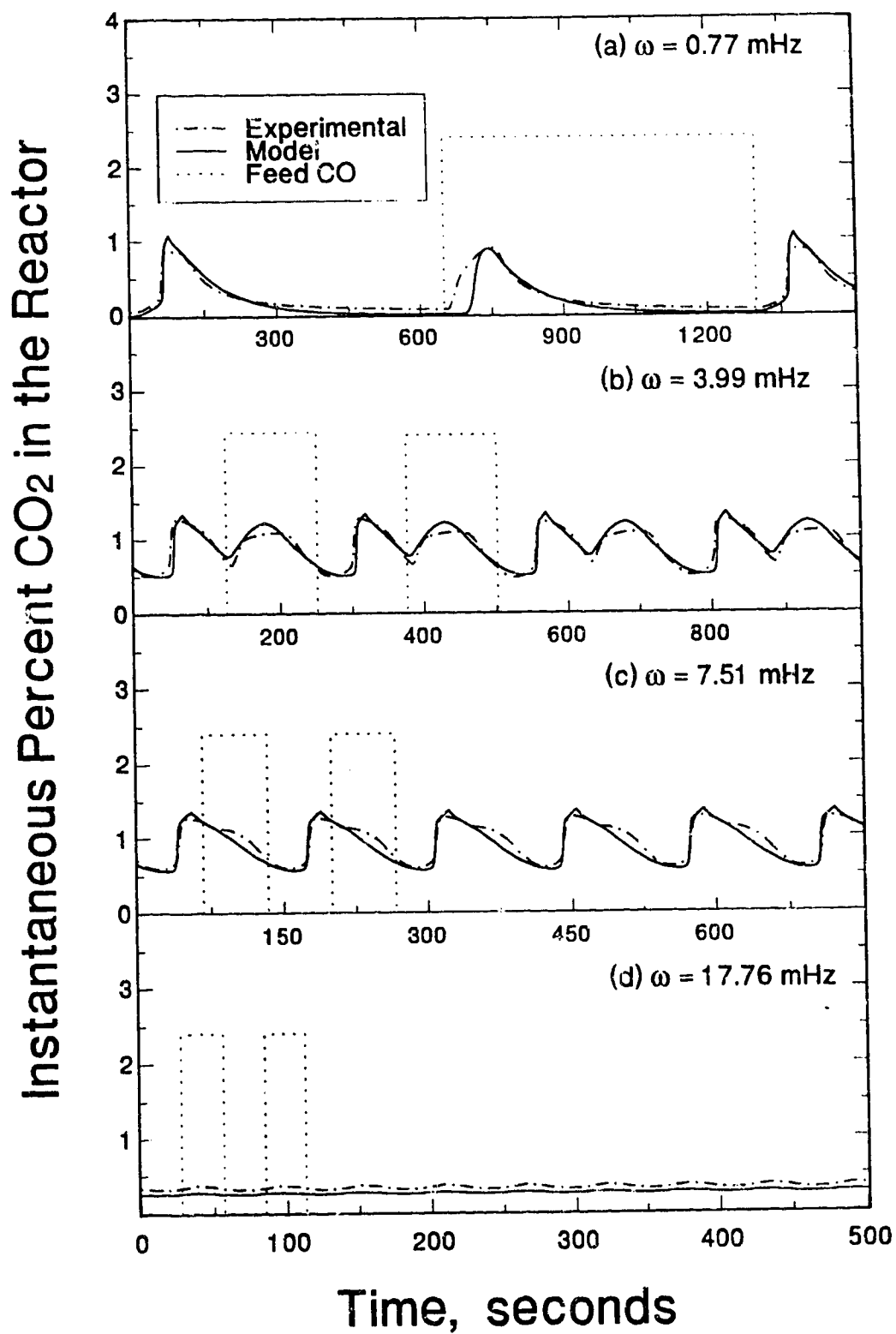
Figure 3.4 Dynamic CO_2 Response During 180° Out-of-Phase Feed
Composition Cycling

3.3). As the gas-phase CO is depleted via transport out of the reactor, more active sites become available on the catalyst surface for N_2O dissociative adsorption. When sufficient active surface sites are available for N_2O dissociation, the CO_2 concentration rises rapidly and reaches a peak value. The reactor CO_2 concentration then decreases as the gas-phase CO is depleted and the adsorbed CO is removed by reaction. The catalyst surface then becomes covered with adsorbed oxygen by the end of the N_2O half-cycle.

When CO is switched on, and N_2O is switched off, the CO_2 concentration increases rapidly. The CO entering the reactor readily reacts with the adsorbed oxygen. After the gas-phase N_2O is completely depleted, the CO_2 concentration drops almost exponentially as the CO cleans the catalyst surface of the remaining adsorbed oxygen. The surface then becomes saturated with adsorbed CO by the end of the CO half-cycle. Typically, two peaks in CO_2 concentration, one in each half-cycle, were observed for frequencies lower than 5 mHz. The CO_2 response at the cycling frequency of 3.99 mHz is shown in Fig. 3.4(b). A comparison of Figs 3.4(a) and (b) shows that the time-average CO_2 concentration is higher at a frequency of 3.99 mHz as compared with that which is obtained at a frequency of 0.77 mHz. The CO_2 concentration does not fall to zero during the long cycles (Fig. 3.4(a)) because of the CO_2 desorption from the alumina support.

As the frequency is increased above 5 mHz. the two peaks in CO_2 concentration per feed cycle began to merge resulting in a single maximum per cycle as shown in Fig. 3.4(c) for a cycling frequency of 7.51 mHz. The magnitude of the CO_2 response to the feed cycling decreased as the frequency was further increased until as can be seen in Fig 3.4(d), at a cycling frequency of 17.76 mHz, the time-average CO_2 concentration was approximately equal to the steady-state value.

The time-average CO conversions for the out-of-phase cycling experiments were calculated from the CO_2 response curves and are given in Fig. 3.5. It is seen that the CO conversion increased almost linearly with increasing frequency up to 4 mHz. This can
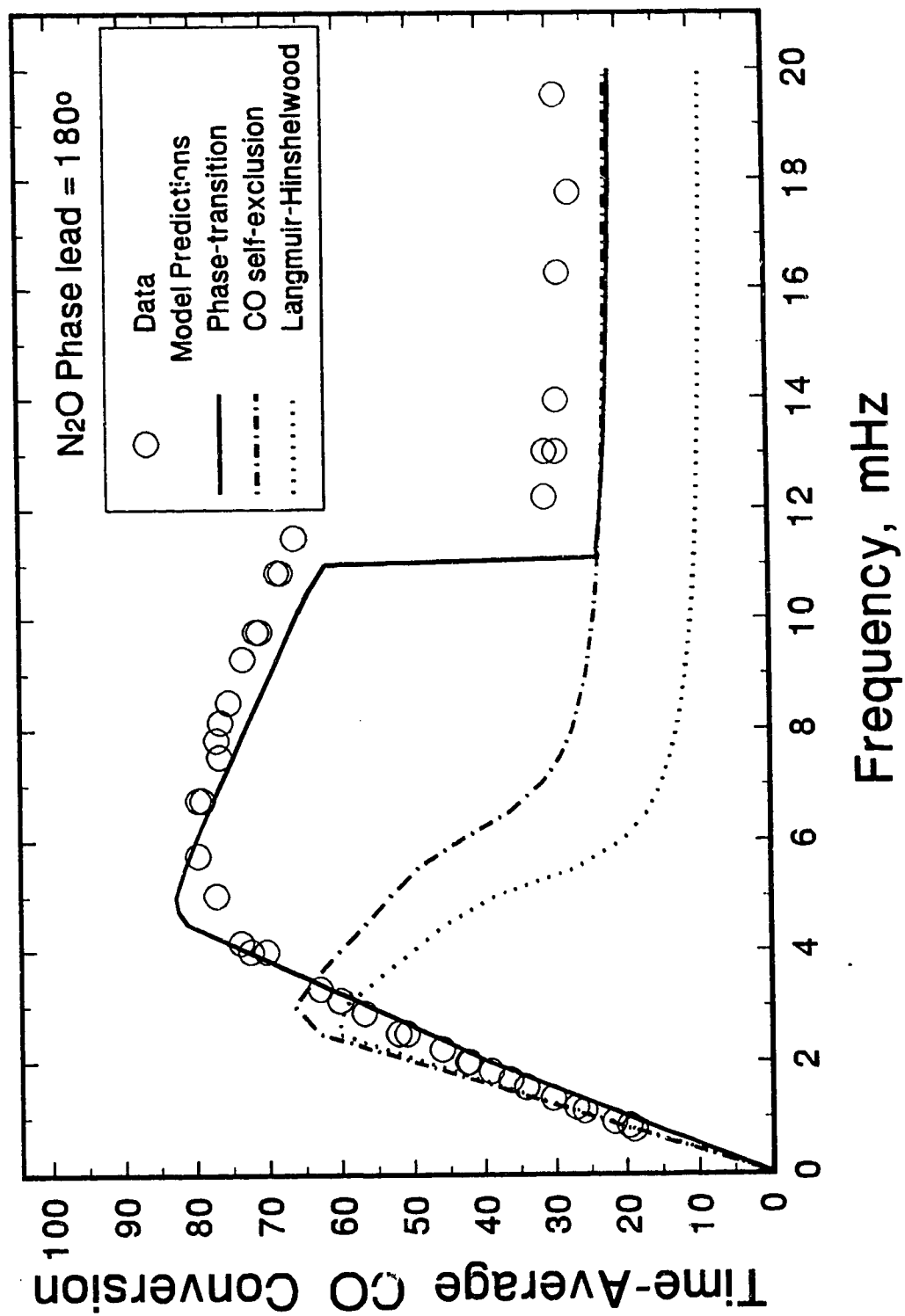
Figure 3.5 Comparison of Model Predictions to Experimental Data of Time-average Conversion for Out-of-Phase Cycling.

be explained in a manner similar to that which was used to explain the CO conversion for the $CO+O_2$ reaction during out-of-phase cycling by Graham and Lynch (7). At low frequencies, two peaks of CO_2 concentration per cycle (Fig. 3.4(a)) were observed and the areas under the curve for each half-cycle were approximately equal. The CO_2 production in each half-cycle can be estimated by considering the surface reaction of a monolayer of adsorbed species (CO or oxygen) plus complete reaction of one reactor volume of gas-phase species (CO or N_2O). The total CO_2 production per cycle is almost constant for all of the low frequencies. Because the CO feed per cycle is equal, CO conversion is therefore, linearly proportional to the frequency of cycling. Thus, the time-average CO conversion at low frequencies can be estimated by:

$$f_{TA} = \frac{(2a_mL_m + 2V[N_2O]_o)}{Q_o[CO]_o} 100\omega \tag{3.1}$$

A comparison of the prediction of time-average CO conversion from equation (3.1) with the experimental data is presented in Fig. 3.6 for frequencies t 2.5 mHz. As can be seen from Fig. 3.6, the predictions match the experimental results for frequencies lower than 1.25 mHz. However, the predicted conversion from equation (3.1) is higher than the experimental values for frequencies above 2.5 mHz due to the incomplete saturation of the surface at the higher frequencies.

As can be seen from Fig. 3.5, the highest CO conversion of 79.5% was obtained at a frequency of 6.7 mHz, and it is approximately four times the steady-state conversion. As the frequency exceeded approximately 12 mHz, the time-average CO conversion abruptly dropped to a low value of 28%. At high frequencies, the gas phase CO and N_2O concentrations are always in the region of feed compositions which give low conversion steady-states (Fig. 3.3). The gas-phase CO concentration does not decrease significantly even by the end of the N_2O half-cycle, and therefore the catalyst surface is always highly covered with adsorbed CO during high frequency feed cycling which leads to a low time-average CO conversion. The critical frequency at which a transition in the
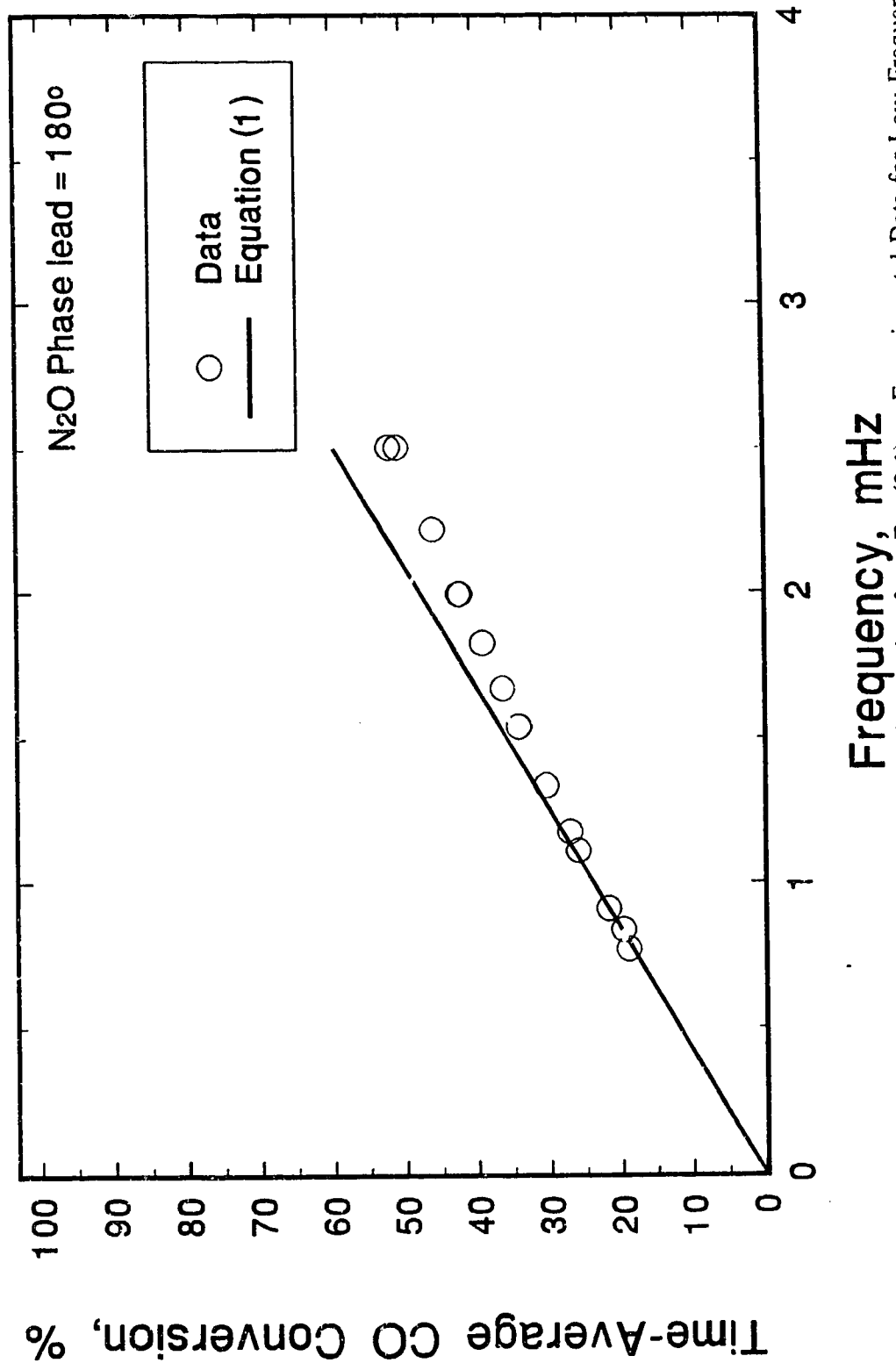
Figure 3.6 Comparison of Predictions of Time-Average Conversion from Eq. (3.1) to Experimental Data for Low Frequency Out-of-Phase Cycling.

time-average CO conversion occurs from a high value to a low value can be estimated from the steady-state bifurcation behavior of the reaction, as demonstrated elsewhere (7). The critical frequency for these out-of-phase cycling experiments lies between 11.5 and 12.2 mHz.

3.3.2 N_2O Phase leads of 90° and 270°

In the second part of the study, the experiments were carried out with N_2O phase leads of 90° and 270°, respectively, over a cycling frequency range of 0.1 to 20 mHz. The N_2O phase lead of 270° is equivalent to a CO phase lead of 90°. The time-average CO conversions are summarized in Fig. 3.7. For frequencies lower than 8 mHz, the time-average CO conversions for feed cycling with 90° N_2O phase lead were generally higher than those observed for 270° N_2O phase lead.

For the 90° N_2O phase lead cycling, the time-average CO conversion rose rapidly with increasing frequency up to 0.25 mHz. For frequencies between 0.25 and 3 mHz, the time-average CO conversion was approximately proportional to the cycling frequency. The highest time-average conversion of 93% was obtained at a frequency of 4.5 mHz, although a value of approximately 90% was found over the entire frequency range of 4 to 6.5 mHz within the accuracy of measurement. At a critical frequency of 8 mHz, the time-average CO conversion dropped abruptly from 88% to 25%.

For feed cycling with an N_2O phase lead of 270°, a linear relationship between the cycling frequency and the time-average CO conversion was observed over the frequency range of 0.2 to 2 mHz. The highest conversion of 52% was obtained at a frequency of 3.33 mHz for the feed cycling with 270° N_2O phase lead. In the critical frequency range, the conversion dropped from 36% at 8.33 mHz to 25% at 9.1 mHz. A comparison of Fig. 3.5 and Fig. 3.7 shows that the highest CO conversion for an N_2O phase lead of 180° lies between the highest CO conversions obtained for 90° (93%) and 270° (52%) N_2O phase leads, respectively.
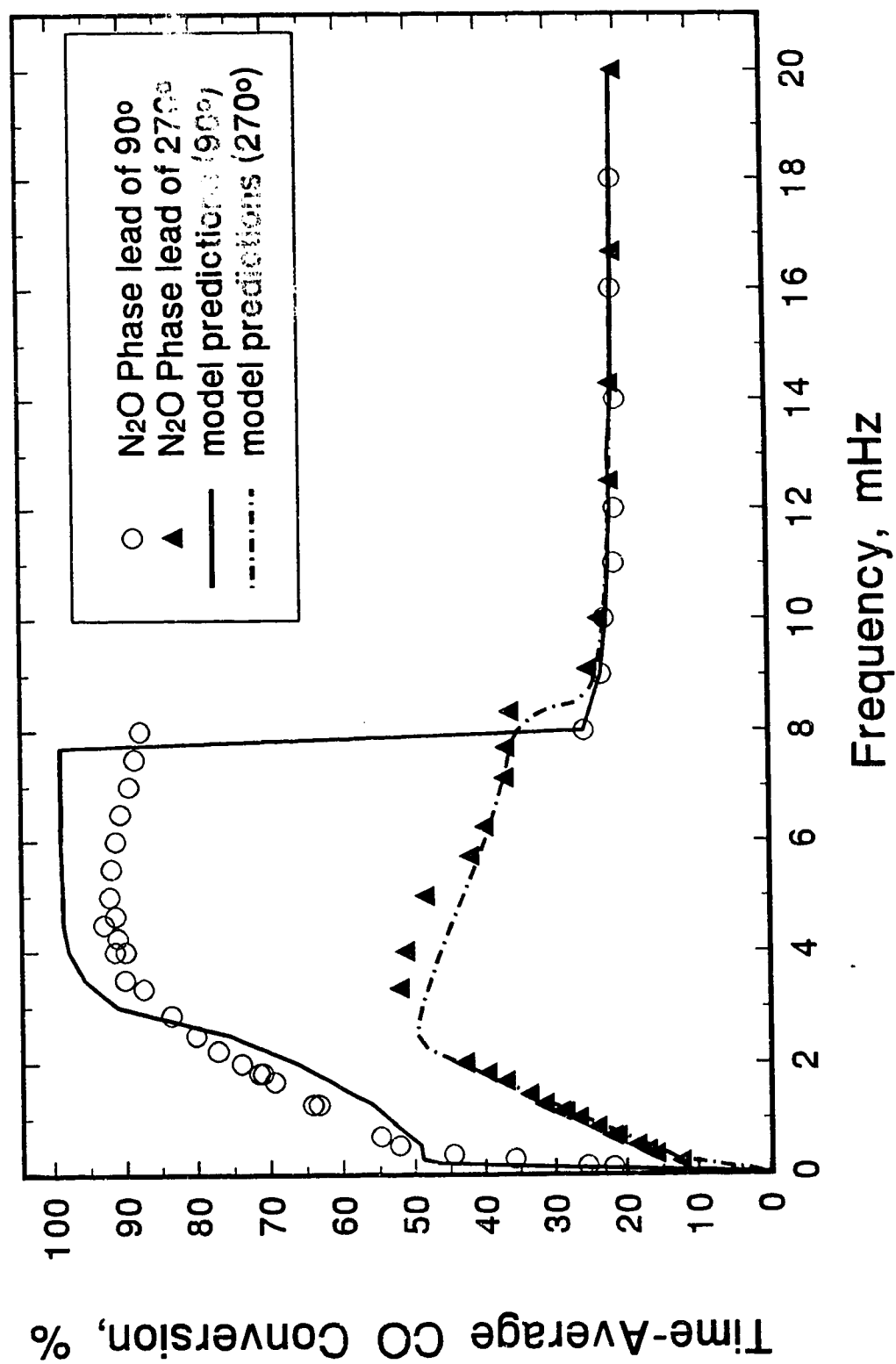
62

Figure 3.7 Effect of Cycling Frequency on Time-Average CO Conversion for N_2O Phase Leads of $90°$ and $270°$.

63

The CO$_2$ response curves at a frequency of 1.25 mHz are shown by the dashed lines in Fig. 3.8 for feed cycling with N$_2$O phase leads of 90° and 270°, respectively. An examination of these CO$_2$ response curves in Fig. 3.8 provides an explanation for high CO conversions obtained for 90° N$_2$O phase lead cycling. A comparison of Figs. 3.8(a) and (b) shows that both the cycles can be divided into four quadrants, each with feed containing only CO, both CO and N$_2$O, only N$_2$O, and no CO or N$_2$O (blank feed), respectively, although the sequence of these quadrants is different for Figures 3.8(a) and 3.8(b). For 90° N$_2$O phase lead cycling, the ed containing only N$_2$O in the first quadrant removes the residual adsorbed CO from the previous blank-feed cycle and therefore the CO$_2$ production in the first quadrant is limited. The surface is saturated with oxygen by the end of the first quadrant. In the second quadrant of the cycle, the feed CO readily adsorbs on the surface saturated with adsorbed oxygen and a high reaction rate is obtained. Almost 50% of the total CO$_2$ production occurs in the second quadrant of the cycle. In the third quadrant, the feed containing only CO reacts with the residual N$_2$O from the previous quadrant. The reaction rate decreases as the N$_2$O is depleted. By the end of the third quadrant, the surface is again saturated with adsorbed CO. In the fourth quadrant, the CO$_2$ desorbs from the alumina support. Some of the adsorbed CO also desorbs in the fourth quadrant due to the very low partial pressure of CO in the reactor. Therefore, the CO$_2$ production in the first quadrant is limited due to the residual adsorbed CO.

When the feed is cycled with an N$_2$O phase lead of 270°, the first quadrant of the cycle has a feed containing both CO and N$_2$O. However, the CO$_2$ production is very small. This is because the catalyst surface is saturated with adsorbed CO from the previous (fourth) quadrant with CO-only feed. Therefore, for a sufficiently long cycle, the CO conversion in this quadrant will be equal to the steady-state conversion of 20%. In the second quadrant, when CO is switched off (feed containing only N$_2$O), the gas-phase N$_2$O does not readily dissociate on the CO-saturated catalyst surface. As the adsorbed CO gradually reacts, sufficient active sites become available for N$_2$O dissociation and the reaction rate increases rapidly as evident by a sharp CO$_2$ peak in this
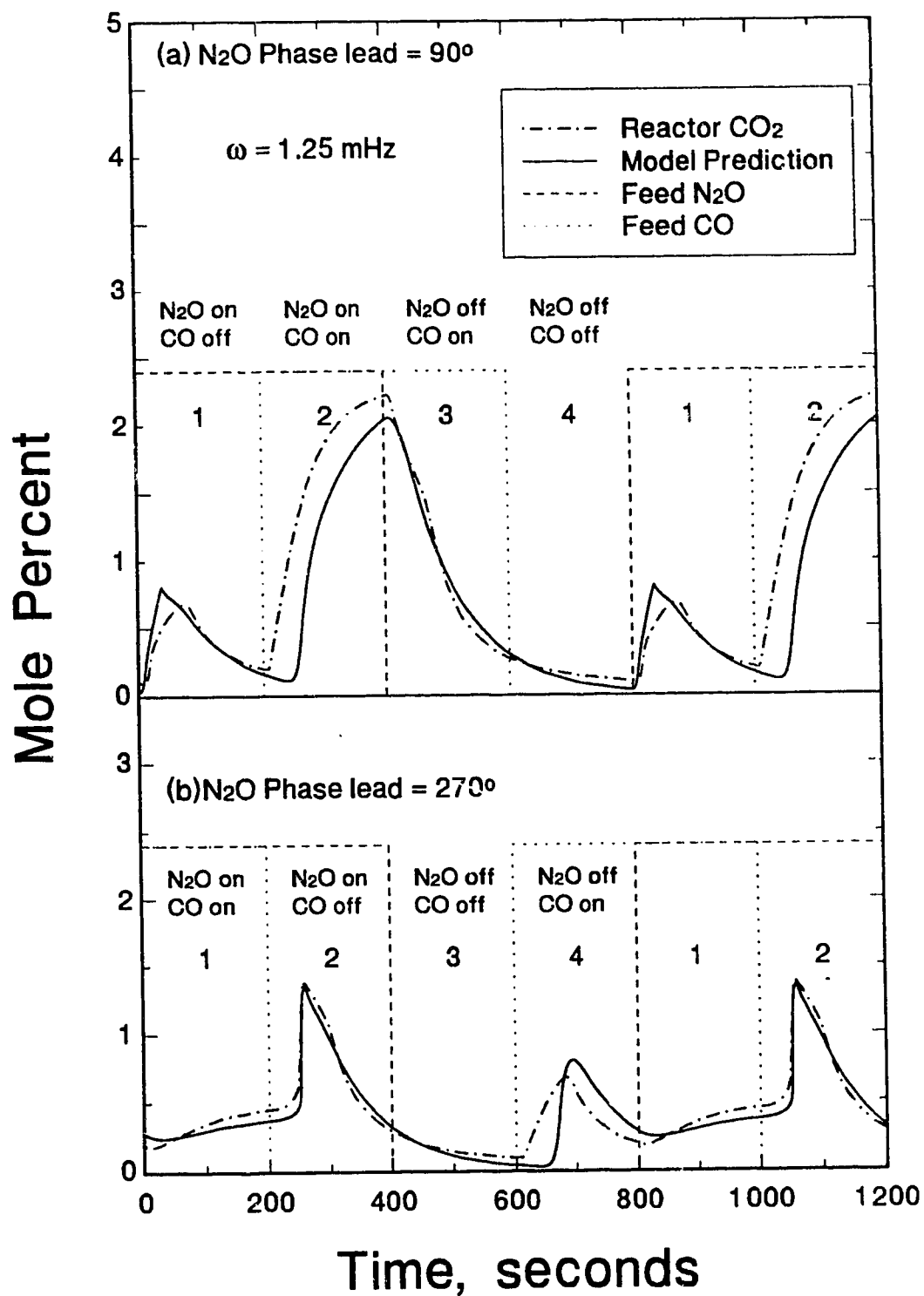
64

Figure 3.8 Dynamic CO_2 Response for 90° and 270° N_2O Phase-Lead.

65

quadrant. The catalyst surface is covered by adsorbed oxygen by the end of the second quadrant. In the third quadrant, the feed does not contain either CO or N_2O and therefore the CO_2 production is mainly due to desorption from the alumina support. In the fourth quadrant, the feed contains only CO which reacts with the residual adsorbed oxygen from the previous quadrant. The CO_2 production is limited by the amount of residual adsorbed oxygen at the beginning of the fourth quadrant.

The main difference between Figs 3.8(a) and (b) is the CO_2 production in the over-lap quadrant of the cycle with feed containing both CO and N_2O. The catalyst surface is saturated with adsorbed oxygen at the beginning of the over-lap quadrant for an N_2O phase lead of 90° and a high reaction rate is obtained. On the other hand, the catalyst surface is saturated with adsorbed CO at the beginning of the over-lap quadrant for an N_2O phase lead of 270° and this leads to a low reaction rate. A very similar phenomenon was observed at several other frequencies over the range of 0 to 7.7 mHz. It can therefore be generalized that, for frequencies lower than the critical frequency, the time-average CO conversion will be higher for N_2O phase leads of less than 180°, as compared with that which is obtained with N_2O phase leads of greater than 180°.

3.3.3 Variable Phasing of Inputs

In the earlier experiments, the effect of cycling frequency on the time-average CO conversion was studied for three values of N_2O phase lead of 90°, 180°, and 270°, respectively. To determine the effect of phase-angle on the time-average conversion, the experiments were carried out by varying the N_2O phase lead between 0° and 360° while holding the cycling frequency constant. The results of the experiments carried out at five different frequencies are summarized in Fig. 3.9.

At a low frequency of 2 mHz (Fig. 3.9(a)), the time-average CO conversion increased rapidly with increasing N_2O phase lead between 10° and 40°. The highest CO conversion of 93.5% was obtained at 40° phase lead. The time-average CO conversion
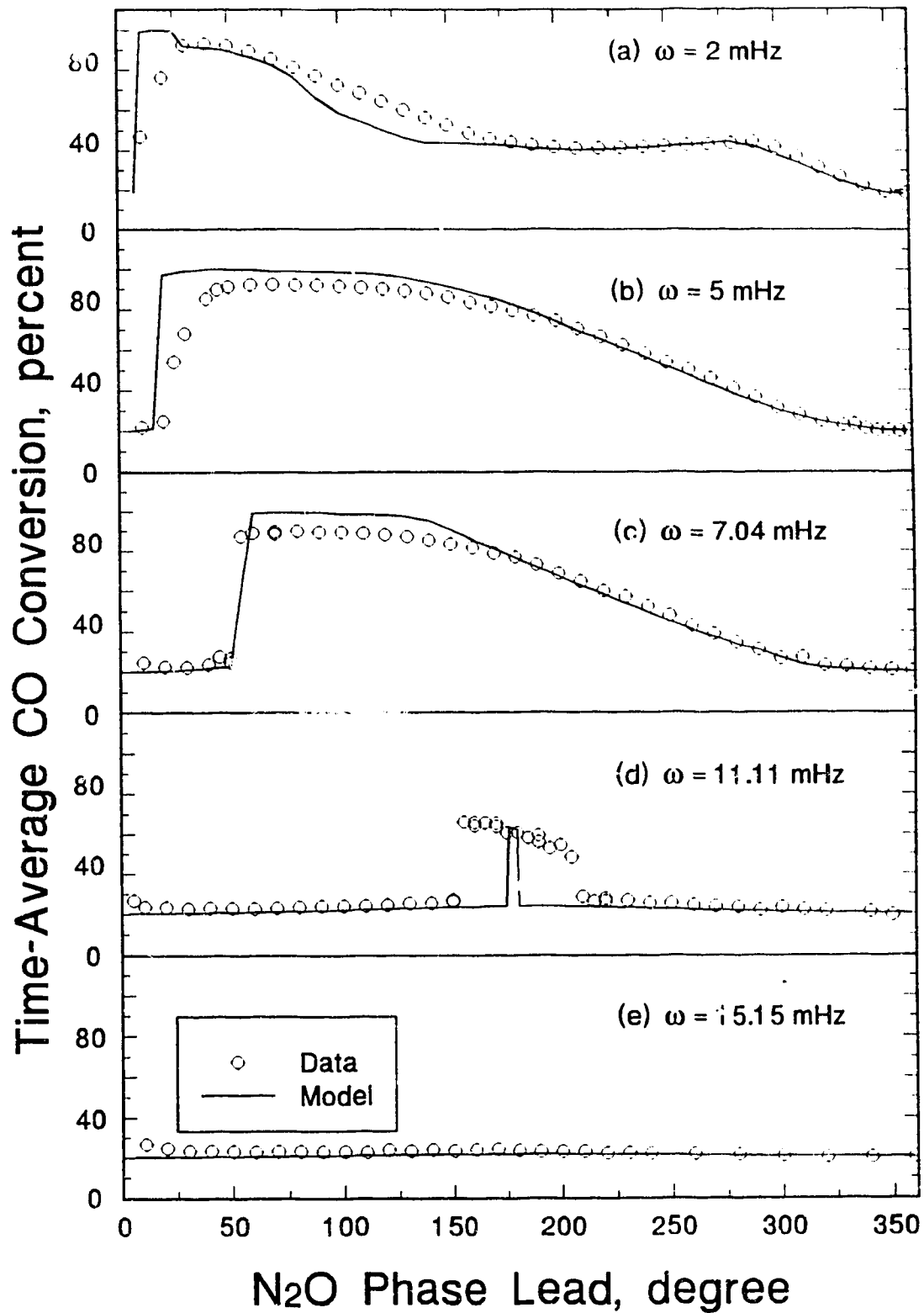
Figure 3.9 Effect of N_2O Phase-Lead on the Time-Average CO Conversion
During Cycling.

then decreased with increasing N_2O phase leads between 50° and 180°. The time-average conversion was approximately constant at 42% over the range of phase-leads between 180° and 300°. The conversions in the range of phase-leads between 180° and 300° can also be estimated by equation (3.1) without significant error, as demonstrated for the out-of-phase cycling in Fig. 3.5. The time-average conversions decreased sharply as the phase-lead was increased above 310°. The experimental observations of Fig. 3.9(a) also support the earlier generalization that relatively high time-average conversions are obtained for N_2O phase leads of less than 180°.

For feed cycling at 5 mHz, as shown in Fig. 3.9(b), the time-average CO conversion was approximately equal to its steady-state value of 20% at small phase-leads of 10° to 20°, and then rose sharply as the phase-lead was increased to 45°. A high time-average conversion of between 80 and 92.5% was attained over a wide range of phase-leads of 50° to 180°. An increase in phase lead above 180° caused the time-average conversion to drop gradually and eventually reached its steady-state value for phase-leads of 320° to 360°. A very similar behavior was also observed at a cycling frequency of 7.04 mHz (Fig. 3.9(c)) except that the span of phase-leads over which high conversions were obtained was narrower than that encountered at 5 mHz. The other significant difference between Figs 3.9(b) and (c) is that the size of the regions of near-steady-state conversion increased as the frequency increased. As the frequency was increased further to 11.11 mHz (Fig. 3.9(d)), the rate enhancement was obtained only for a narrow range of phase-leads (155° to 205°). For a high frequency of 15.15 mHz, the time-average conversion was approximately equal to its steady-state value for all phase-leads as shown in Fig. 3.9(e).

The CO_2 response curves for a cycling frequency of 5 mHz, at five different N_2O phase leads are shown by dashed lines in Fig. 3.10. For phase-leads of 10° and 330°, there is a significant overlap of CO and N_2O feed cycles, so that the gas-phase composition in the reactor is always in the low-conversion region (Fig. 3.3(a)) characterized by a catalyst surface saturated with adsorbed CO. Therefore, the low
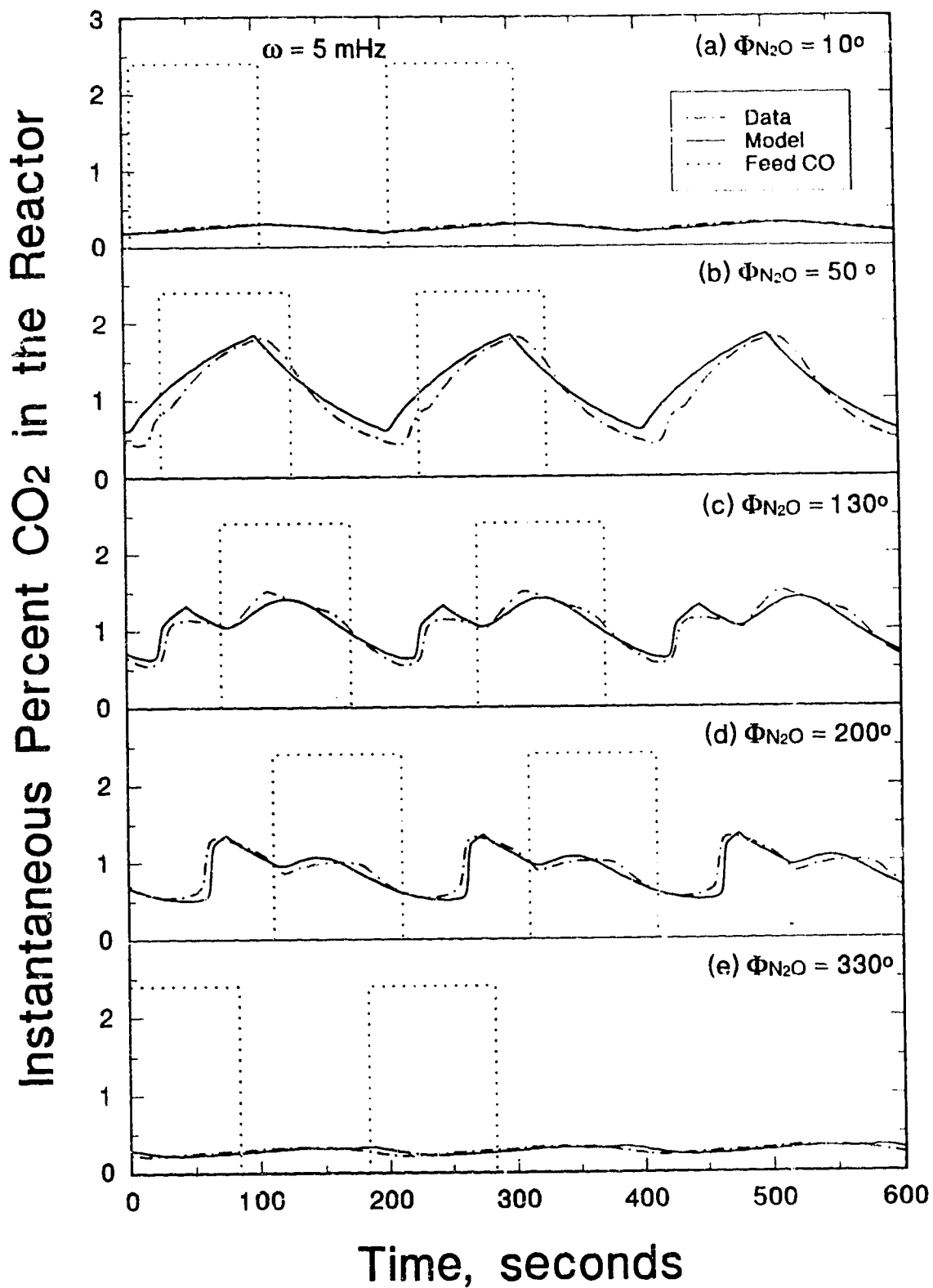
Figure 3.10 Effect of N_2O Phase-Lead on the Dynamic CO_2 Response.

reaction rates result in relatively flat CO_2 curves, as shown in Figs 3.10(a) and (e). For phase-leads of 50° and 130°, sufficient time is available for reacting away most of the adsorbed CO and the catalyst surface is saturated by adsorbed oxygen before the CO and N_2O feed cycles overlap. Therefore, high reaction rates are obtained in the region of CO and N_2O overlap, as characterized by the large peaks of CO_2 in Figs 3.10(b) and (c). A comparison of Figs 3.10(c) and (d) shows that the major CO_2 peak occurs in the CO-N_2O overlap part of the cycle for 130° phase lead and in the N_2O-only part of the cycle for 200° phase-lead. The differences between Figs 3.10(c) and (d) are very similar to the differences in Figs 3.8(a) and (b), for which an explanation was given earlier.

From these experiments it is apparent that the maximum time-average conversion can be obtained for an appropriate combination of N_2O phase lead (less than 180°) and cycling frequency. In this study the highest time-average CO conversion of 93.5% was attained at a frequency of 2 mHz with an N_2O phase-lead of 40°. In general, a certain overlap of the CO and N_2O cycles gives a time-average conversion which is higher than the highest conversion obtained for the out-of-phase cycling, particularly for the intermediate frequency range of 2 to 7 mHz. These observations are consistent with the findings of Graham and Lynch for the $CO+O_2$ reaction (7).

3.4 Mathematical model

A mathematical model for the reaction processes must be able to describe the dynamic behavior of the reaction and the rate enhancements observed in this study as well as the steady-state multiplicity discussed in Chapter 2. As a starting point, the steady-state model which was earlier used to describe the multiplicity behavior was re-cast in a dynamic form to determine if description of the reaction dynamics was possible.

3.4.1 CO Self-exclusion Model

In Chapter 2, the steady-state multiplicity of the N_2O+CO reaction over an alumina

70

supported Pt catalyst was described by a model incorporating carbon monoxide self-exclusion from the platinum surface. The proposed reaction mechanism consisted of the following three elementary steps.

$$CO(g) \; + \; M \; \rightleftharpoons \; M-CO \qquad\qquad (3.2)$$

$$N_2O(g) \; + \; M \; \rightarrow \; N_2(g) \; + \; M-O \qquad\qquad (3.3)$$

$$M-CO \; + \; M-O \; \rightarrow \; CO_2(g) \; + \; 2M \qquad\qquad (3.4)$$
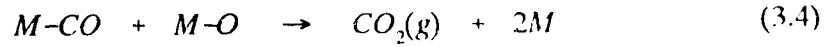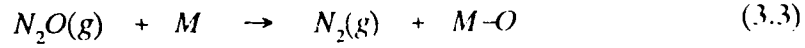
It was shown that the CO self-exclusion effect could describe the experimental low-conversion steady-state results. The CO self-exclusion effect requires that an adsorbed CO molecule exclude other CO molecules from an area equivalent in size to N_{co} surface Pt atoms, where N_{CO} is slightly greater than unity.

The reactor used in this study can be modelled a: . . . .' CSTR due to the high recycle ratio that was employed. As previously shown in Chapter 2, the internal diffusion and external mass transfer resistances are negligible under the experimental conditions used in this study. Thus, mass balances on the gas-phase and surface species produce the following six dimensionless ordinary differential equations, where all symbols are defined in the **Notation** section.

$$\frac{dX}{d\tau} = X_o - Q_n X - K_1 X(1 - \theta_{CO} - \theta_o)\frac{(1 - N_{co}\theta_{co})}{(1 - \theta_{CO})} + K_{-1}\theta_{co} \qquad\qquad (3.5)$$

$$\frac{dY}{d\tau} = Y_o - Q_n Y - K_2 Y(1 - \theta_{CO} - \theta_o) \qquad\qquad (3.6)$$

$$\frac{dZ}{d\tau} = Z_o - Q_n Z + K_3 \theta_{co}\theta_o - K_4 Z(1 - \xi_{co}) + K_{-4}\xi_{co} \qquad\qquad (3.7)$$

71

$$\frac{d\theta_{co}}{d\tau} = \alpha_m[K_1X(1 - \theta_{co} - \theta_o)\frac{(1 - N_{co}\theta_{co})}{(1 - \theta_{co})} - K_{-1}\theta_{co} - K_3\theta_{co}\theta_o] \tag{3.8}$$

$$\frac{d\theta_o}{d\tau} = \alpha_m[\frac{F_{N_2O}}{F_{co}}K_2Y(1 - \theta_{co} - \theta_o) - K_3\theta_{co}\theta_o] \tag{3.9}$$

$$\frac{d\xi_{co_2}}{d\tau} = \alpha_s[K_4Z(1 - \xi_{co_2}) - K_{-4}\xi_{co_2}] \tag{3.10}$$

where

$$Q_n = 1 - F_{co}[K_1X(1 - \theta_{co} - \theta_o)\frac{(1 - N_{co}\theta_{co})}{(1 - \theta_{co})}$$
$$-K_{-1}\theta_{co} - K_3\theta_{co}\theta_o + K_4Z(1 - \xi_{co_2}) - K_{-4}\xi_{co_2}] \tag{3.11}$$

Equations (3.5) to (3.10) can be used to describe the steady-state behavior by setting the time-derivatives in the equations to zero and solving the resulting algebraic equations. For steady-state operation, $X_o=1$, $Y_o=1$, and $Q_n=1$, and in addition $Z_o=0$ for all conditions because CO_2 was not present in the feed. The values of the kinetic parameter K_1, K_{-1}, K_2 and K_3 must be selected so as to describe all of the time-average CO conversions during cycling experiments as well as the steady-state multiplicity data from the earlier experimental study (4). The time-average CO conversion is not affected by the adsorption and desorption of CO_2 on the alumina support Therefore, in initial attempts at determining appropriate values of the kinetic

parameters, the values of the CO_2 adsorption and desorption rate constants, K_i and K_i were set equal to zero while calculating time-average CO conversions. Further simplification of the model was made by setting Q_n equal to unity because of the low values of the gas-phase concentrations used in this study. The set of five differential equations (3.5)-(3.9) was integrated over several cycles, using a variable step-size fourth-order Runge-Kutta-Fehelberg method to calculate the time average CO conversion during feed composition cycling.

Integration was always performed using the initial conditions $X=Y=Z=\theta_{CO}=\theta_O=0$. During composition cycling, the dimensionless feed concentrations of CO and N_2O, X_o and Y_o, respectively, have values of either 2 or 0, as given by the following conditions for the nth cycle:

for all values of ϕ_{N_2O}

$$Y_o = 2, \qquad (n-1)\tau_c \leq \tau < (n-\tfrac{1}{2})\tau_c \qquad (3.12)$$

$$Y_o = 0, \qquad (n-\tfrac{1}{2})\tau_c \leq \tau < n\tau_c \qquad (3.13)$$

for $0^\circ \leq \phi_{N_2O} < 180^\circ$

$$X_o = 0 \qquad (n-1)\tau_c \le \tau < (n-1+\frac{\phi_{N_2O}}{360})\tau_c \qquad (3.14)$$

$$X_o = 2 \qquad (n-1+\frac{\phi_{N_2O}}{360})\tau_c \le \tau < (n-\frac{1}{2}+\frac{\phi_{N_2O}}{360})\tau_c \qquad (3.15)$$

$$X_o = 0 \qquad (n-\frac{1}{2}+\frac{\phi_{N_2O}}{360})\tau_c \le \tau < n\tau_c \qquad (3.16)$$

for $180° \le \phi_{N_2O} < 360°$

$$X_o = 2 \qquad (n-1)\tau_c \le \tau < (n-\frac{3}{2}+\frac{\phi_{N_2O}}{360})\tau_c \qquad (3.17)$$

$$X_o = 0 \qquad (n-\frac{3}{2}+\frac{\phi_{N_2O}}{360})\tau_c \le \tau < (n-1+\frac{\phi_{N_2O}}{360})\tau_c \qquad (3.18)$$

$$X_o = 2 \qquad (n-1+\frac{\phi_{N_2O}}{360})\tau_c \le \tau < n\tau_c \qquad (3.19)$$

The attainment of cycle invariance was determined according to the procedures described by Lynch (13). When several sequential integrations were performed, i.e., ω varied, ϕ_{N_2O} varied, etc., the initial conditions for successive integrations were based on the final state of the immediately preceding converged cycle.

The initial estimates of the kinetic parameters were obtained from the values used to describe the steady-state multiplicity behavior (4). It was found that the model predictions for time-average CO conversion for the feed cycling were considerably lower than the experimental data. The model predictions for time-average CO conversions for feed cycling could be improved by increasing the values of rate parameters K_2 and K_3.

However, increasing the values of K_2 and K_3 necessitated the change of other parameters in order to maintain agreement with the steady-state data. In particular, it was necessary to reduce the value of the CO self exclusion factor, N_{co}, in order to be able to describe the experimental low-conversion steady-state data and the low-to-high conversion bifurcation points for high values of K_2 and K_3. However, the large values of K_2 and K_3 also resulted in significant model-experimental discrepancies in the values of feed CO% at which high-to-low conversion bifurcation occurs for steady-state experiments. While maintaining a complete model-experimental agreement for the steady-state data, it was possible to vary the values of K_2 and K_3 only marginally when attempting to improve the predictions of the time-average CO conversions during feed cycling. Over large regions of parameter space, the values of the CO adsorption and desorption rate parameters, K_1 and K_{-1}, did not have any significant effect on model predictions as long as the ratio of K_1 to K_{-1} was maintained constant. The main effect of lower values of K_1 and K_{-1} was a reduction in the number of integration steps needed for solving the differential equations. Therefore, in order to prevent the computational requirements from becoming unmanageable, relatively low values of K_1 and K_{-1} (while holding the ratio constant) were always used. A low value of K_1 implies a correspondingly low value of the CO sticking probability, S_{CO}. Therefore, the values of K_1, K_{-1} and S_{CO} used in this study are lower than the values used in Chapter 2 as can be seen from Table 3.1. It is possible to increase arbitrarily the value of S_{CO} by one or more orders of magnitude (with a corresponding increase in $k_{-1}°$ to keep K_1/K_{-1} constant) without significantly affecting the predictions from the model.

The predictions of the time-average CO conversion for out-of-phase feed cycling from the CO self-exclusion model are shown by the dashed line in Fig. 3.5, where it can be seen that the model predictions approximately match the experimental data at frequencies below 3 mHz and at high frequencies above 11 mHz. In order to describe as much of the dynamic data as possible while maintaining a near complete agreement with the steady-state data from Chapter 2, it was also necessary to use different values of the other rate parameters, namely, K_2, K_3 and N_{CO}, as shown in Table 3.1. As

discussed earlier, the time-average conversion for the low frequencies can be estimated reasonably accurately by equation (3.1) and therefore, is relatively insensitive to the reaction mechanism model. However, the model predictions are consistently lower than the experimental data for the intermediate frequency range of 2 to 11 mHz. The effect of CO self-exclusion is illustrated by setting N_{CO} equal to unity as shown by the dotted line in Fig. 3.5. As can be seen from Fig 3.5, the time-average CO conversions predicted from a Langmuir-Hinshelwood type model (N_{CO}=1) are consistently lower than those predicted by the CO self-exclusion model, particularly for frequencies higher than 11 mHz. This observation is consistent with the earlier study (4) where only the CO self-exclusion effect could account for the experimentally observed CO conversions for the unique low-conversion steady-state. Therefore, CO self-exclusion was considered as an integral part of the further model development. In order to describe the high values of time-average conversion during feed cycling experiments, as well as the steady-state multiplicity, it was necessary to use a surface phase transformation model similar to that described by Lynch et al. (7,18).

Table 3.1

Model Parameters at 499 K

| Parameter	CO Self-Exclusion Model	Surface-Phase Transition Model	Chapter 2 Mechanism 4
K_1	28,000	28,000	2,604,422
K_{-1} (1% CO feed)	100	15.75 ($\psi_2 = 1$)	7,395
K_2	18	23.6	37.8
K_3 (1% CO feed)	20	20 ($\psi_3 = 1$)	15.46
S_{CO}	1.076×10^{-4}	1.076×10^{-4}	1×10^{-2}
L_m	2×10^{-5}	1.42×10^{-5}	2×10^{-5}
N_{CO}	1.018	1.0015	1.025

3.4.2 Surface-Phase Transformation Model

It has been shown that a clean Pt(100) surface undergoes a reconstruction from a (1x1) structure to a quasi-hexagonal order corresponding to a complicated (5x20) LEED pattern (19) which appears to be the thermodynamically favoured structure (20). Numerous studies (21-26) have shown that the reconstruction [(5x20) LEED pattern] exhibit by the clean Pt(100) surface is removed by the adsorbate-induced interaction of CO, O_2, H_2 or NO. Thiel et al. (27) observed that the nucleation of (1x1) patches occurs on the reconstructed (hex) surface of Pt(100) even at a very low CO surface coverage and proceeds until the entire surface has been converted to the (1x1) phase at $\theta_{CO}=0.5$. On the other hand, during CO desorption, the hex-phase does not return until the fractional CO surface coverage is decreased below 0.3. The reconstructed surface (hex phase) is less active as compared to the unreconstructed (1x1) surface. The oxygen sticking probability is low for the surface in hex-phase (26), but is at least two orders of magnitude larger for the (1x1) surface (28). A similar observation is reported by Bonzel et al. (29) for NO adsorption on Pt(100). They observed no adsorption of NO on reconstructed hex-surface at temperatures higher than 380 K. On the other hand, the unreconstructed (1x1) surfaces were able to adsorb NO molecularly up to temperatures of 410 K.

The phenomenon of the adsorbate-induced reversible surface-phase transition for the clean Pt(100) surface, and resulting reaction rate enhancements have been used to describe the kinetic oscillations of the $CO+O_2$ reaction (30) and the $NO+CO$ reaction (31, 32) under high vacuum conditions on well characterized catalyst surfaces. However, to describe the rate oscillations of CO oxidation on supported Pt catalyst and Pt foils at near atmospheric pressure, various other mechanisms have been proposed. For example, a process of slow oxidation and reduction of the catalyst surface (33, 34) has been used to model the rate oscillations of CO oxidation on Pt at atmospheric pressure. It has also been suggested (35) that the formation of platinum oxide is catalyzed by silicon impurities on the supported catalyst. Other studies (36, 37) proposed that a process of slow activation/deactivation of the catalyst surface due to diffusion of carbon to the surface

77

may be responsible for observed oscillations of CO oxidation on Pt foil at atmospheric pressure. A kinetic model based on the variation of the catalyst surface temperature (38) has also been suggested to describe the self-sustained oscillations of CO oxidation on silica-supported Pt pellets at atmospheric pressure. Nevertheless, the Pt(100) surface transformation phenomenon has been successfully used (18) to describe the self-sustained oscillations of CO oxidation on alumina-supported Pt catalyst at atmospheric pressure. A similar mechanism has also been suggested (39) for oscillations of NO+CO reaction on polycrystalline Pt-Al$_2$O$_3$ catalyst in FTIR spectroscopic investigations. Schwartz and Schmidt (31) suggested that the adsorbate induced 1x1↔hex surface-phase transition may be operative on supported Pt catalysts because in many reactive gases all crystallographic orientations tend to facet into predominantly (100) crystal planes. Wang et al. (40) have shown that supported platinum crystallites form predominantly (100) crystal planes when grown in hydrogen. These studies lend support to the model based on Pt(100) surface-phase transition to describe the rate oscillations on supported Pt catalyst. Graham and Lynch (7) used the surface-phase transformation effect to describe the complex behavior, including steady-state multiplicity and reaction rate enhancement during feed cycling, of the CO+O$_2$ reaction on an alumina-supported Pt catalyst at atmospheric pressure. Because of the apparent similarity of the CO+N$_2$O and CO+O$_2$ reaction systems, the same surface-phase transformation phenomenon has been used in this study to describe reaction rate enhancement for the CO+N$_2$O reaction during feed cycling.

As shown by Graham and Lynch (7), the use of the surface-phase transformation model requires that the rate constants for oxygen adsorption and surface reaction with CO depend on the CO surface coverage in a very nonlinear fashion. A graphical representation of the reversible surface-phase transition due to CO adsorption is shown in Fig. 3.11 for the N$_2$O+CO reaction. It is assumed that the catalyst surface is in phase-1 at low CO surface coverage. Phase-1 is a low activity phase similar to the reconstructed quasi-hexagonal phase of Pt(100). The catalyst surface remains in phase-1 until the fractional CO surface coverage reaches a high critical value of 0.95, when the entire surface is instantaneously transformed into phase-2. Phase-2 is a high activity phase

78
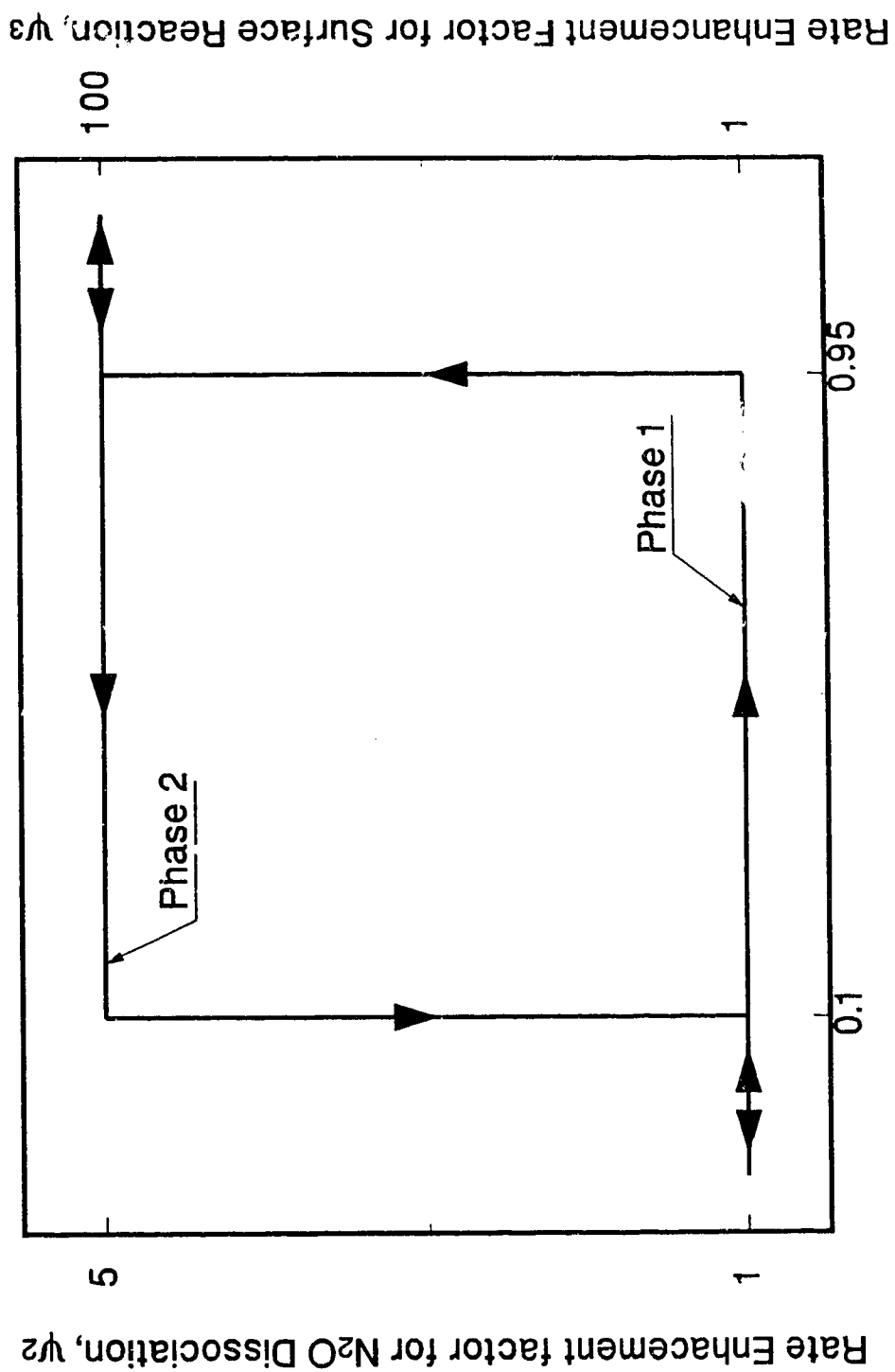
Figure 3.11 Reaction Rate Enhancement due to CO-Adsorbate Dependent Pt Surface-Phase Transition.

similar to the unreconstructed (1x1) phase of Pt(100). In phase-2, the N_2O dissociation rate constant, k_2, and the surface reaction rate constant, k_3, have high values relative to phase-1. The surface remains in phase-2 until the fractional CO surface coverage falls to a low critical value of 0.1, when the entire surface is instantaneously transformed back to phase-1. Mathematical formulation of this effect results in k_2 and k_3 being given by:

$$k_2 = \psi_2 k_2^o \exp(-E_2/RT) \qquad (3.20)$$

$$k_3 = \psi_3 k_3^o \exp(-E_3/PT) \qquad (3.21)$$

where ψ_2 and ψ_3 are the enhancement factors which are greater than unity (5 and 100, respectively) when the surface is in the (1x1) phase (high CO coverage). For the reconstructed (5x20) phase (low CO coverage), $\psi_2=1$ and $\psi_3=1$ always holds. For intermediate coverage between $\theta_{CO}=0.1$ and $\theta_{CO}=0.95$, the values of ψ_2 and ψ_3 depend on the prior state of the surface as shown in Fig. 3.10.

Graham and Lynch (7) used the same value of 250 for the enhancement factors for the (1x1) phase for both the surface reaction rate constant and the oxygen sticking probability. In this study a lower value of $\psi_2(=5)$ as compared to $\psi_3(=100)$ was sufficient to describe the high time-average CO conversions obtained during the feed cycling experiments. It would therefore appear that the rate enhancement for N_2O dissociation due to hex$\leftrightarrow$(1x1) surface transition is much smaller than the increase of approximately two orders of magnitude for the oxygen sticking probability. This can be attributed to the differences in the adsorption mechanisms of O_2 and N_2O. In a study of comparative adsorption of O_2 and N_2O on recrystallized platinum ribbons using thermal desorption and mass spectrometry, Alnot et al. (41) noted that oxygen adsorption at 300 K leads to three binding states while N_2O adsorption fills only the most energetic one. The sticking coefficient for O_2 dissociative adsorption at 500 K was found to be 0.16 as compared to 0.0068 for N_2O dissociative adsorption. They attributed the differences

between O_2 and N_2O dissociative adsorption to steric factors. Daniel *et al.* (*42*) noted that for a clean Rh(100) surface, the saturation coverage of oxygen is twice as large for O_2 as N_2O. McCabe and Wong (*2*) attributed the lower rate of the $CO+N_2O$ reaction compared to $CO+O_2$ and $CO+NO$ reactions under the conditions characterized by high CO surface-coverage to the lower rate of dissociative adsorption of N_2O as compared to the rate of dissociative O_2 and NO adsorption on alumina-supported Rh catalyst.

The time-average CO conversions were calculated by integrating equations (3.5)-(3.9). In the initial attempts at determining suitable model parameters, the values of K_1, K_{-1}, K_2, K_3 and N_{CO} were chosen so that the model predictions matched the experimental CO conversions both for out-of-phase feed cycling (Fig. 3.5) and for the steady-state experiments at 499 K (Fig. 3.3(a)). The model parameters were then further adjusted so as to describe not only the experimental data for all of the forced composition cycling experiments (Figs 3.5, 3.7 and 3.9) but also the steady-state data from the earlier study (Figs. 3.3(b), 3.3(c) and 3.12). All integrations were carried out over several cycles until the CO conversion per cycle ba... ...O, N_2O and CO_2 matched within 0.2% of each other and did not change for two consecutive cycles. The percent change in the fractional ...erage was used as a criterion as given by equation (3.22).

$$\left| \frac{\theta_o(n\tau_c) - \theta_o((n-1)\tau_c)}{\theta_o((n-1)\tau_c)} \right| \qquad n = 1,2,3\ldots\ldots \qquad (3.22)$$

The model predictions for time-average CO conversions for out-of-phase cycling are shown by the solid line in Fig. 3.5. The initial slope of the conversion-frequency curve is strongly dependent on the ratio of the bulk volume to catalyst surface capacitances (α_m) as demonstrated by Lynch (*14*). Therefore, the value of the catalyst adsorption capacity, L_m, was adjusted down from 2×10^{-5} to 1.42×10^{-5} mol/m^2, to match the predictions with the experimental data for the frequencies lower than 3 mHz. The other kinetic parameter